arXiv:astro-ph/0408411v3 21 Apr 2009

Quiescent Dense Gas in Protostellar Clusters: the Ophiuchus A Core

James Di Francesco[1]

National Research Council of Canada, Herzberg Institute of Astrophysics, 5071 West Saanich Road, Victoria, BC V9E 2E7, Canada

Philippe André

Service d'Astrophysique, CEA/DSM/DAPNIA, C.E. Saclay, 91191, Gif-sur-Yvette Cedex, France

Philip C. Myers

Harvard-Smithsonian Center for Astrophysics 60 Garden St. MS-42, Cambridge, MA, 02138-1516, U.S.A.

ABSTRACT

We present combined BIMA interferometer and IRAM 30 m Telescope data of N_2H^+ 1–0 line emission across the nearby dense, star forming core Ophiuchus A (Oph A) at high linear resolution (e.g., ∼1000 AU). Six maxima of integrated line intensity are detected which we designate Oph A-N1 through N6. The N4 and N5 maxima are coincident with the starless continuum objects SM1 and SM2 respectively but the other maxima are not coincident with previously-identified objects. In contrast, relatively little N_2H^+ 1–0 emission is coincident with the starless object SM2 and the Class 0 protostar VLA 1623. The FWHM of the N_2H^+ 1–0 line, ΔV, varies by a factor of ∼5 across Oph A. Values of $\Delta V < 0.3$ km s^{-1} are found in 14 locations in Oph A, but only that associated with N6 is both well-defined spatially and larger than the beam size. Centroid velocities of the line, V_{LSR}, vary relatively little, having an rms of only ∼0.17 km s^{-1}. Small-scale V_{LSR} gradients of <0.5 km s^{-1} over ∼0.01 pc are found near SM1, SM1N, and SM2, but not N6. The low N_2H^+ abundances of SM2 or VLA 1623 relative to SM1, SM1N, or N6 may reflect relatively greater amounts of N_2 adsorption onto dust grains in their colder and probably denser interiors. The low ΔV of N6, i.e.,

[1]formerly at Radio Astronomy Laboratory, University of California, Berkeley, 601 Campbell Hall, Berkeley, CA, 94720-3411, U.S.A.

0.193 km s^{-1} FWHM, is only marginally larger than the FWHM expected from thermal motions alone, suggesting turbulent motions in the Oph A core have been reduced dramatically at this location. The non-detection of N6 in previous thermal continuum maps suggests that interesting sites possibly related to star formation may be overlooked in such data.

Subject headings: ISM: individual (Oph A) – stars: formation – ISM: abundances – ISM: kinematics and dynamics

1. Introduction

The numbers of embedded clusters observed in giant molecular clouds and the inferred birthrates of their stellar populations suggest strongly that stars in the Galaxy form predominantly within clustered environments and not in isolation (Lada & Lada 2003). At present, however, no paradigm exists describing how stellar formation proceeds within clusters inside turbulent cloud cores (Meyer et al. 2000). Such cores can contain starless objects, i.e., local maxima of arbitrarily high column density where no evidence for star formation has been detected, as well as extremely young protostellar objects, i.e., locations where evidence for star formation has been detected. Observations of these objects in clusters should significantly improve our understanding of how they form. The gas and dust comprising or surrounding these objects can reveal the motions and physical conditions associated with the earliest stages of stellar formation, providing the necessary constraints to new models.

The Ophiuchus star-forming molecular cloud is particularly well suited for an intensive study of the dense gas associated with star formation within clusters. Only 125 pc distant (de Geus, de Zeeuw, & Lub 1989, de Geus 1992), Ophiuchus contains the nearest embedded cluster to the Sun (see Allen et al. 2002, and references therein), residing within high column densities of gas and dust (e.g., see Loren, Wootten, & Wilking 1990; LWW90). Therefore, appropriate observations of Ophiuchus can reveal starless objects and extremely young protostellar objects within a clustered environment at the best possible sensitivities and the finest possible linear resolutions.

Over the last decade, observations of the cores associated with L1688 in Ophiuchus, i.e., Oph A to Oph F (see LWW90), have revealed numerous potential starless and extremely young protostellar objects. In particular, the Oph A core contains a protostellar cluster including the prototypical "Class 0" object, VLA 1623, in addition to starless objects to its north and east named SM1N, SM1, and SM2 (see André, Ward-Thompson, & Barsony 1993; AWB93). Wide-field 1.3 mm continuum maps by Motte, André, & Neri (1998; MAN98)

revealed Oph A is the brightest of the Oph cores, and a multiresolution wavelet analysis of its emission suggested the presence of eight other starless objects in Oph A. The objects A-MM6, A-MM7, and A-MM8, together with SM1N, SM1, and SM2, comprise an arc within the filamentary structure of Oph A centered on the nearby B star S1 (see Figure 2a of MAN98). MAN98 also found the starless objects in the Oph cores have a mass spectrum reminiscent of the stellar IMF, suggesting a link exists between the formation of these objects and actual stars in clusters.

In this paper, we examine emission from dense gas associated with the Oph A core, using combined single-dish and interferometer data to attain a linear resolution of ∼1000 AU. We observed the 1–0 transition of the N_2H^+ molecular ion since it is a tracer of dense gas (e.g., its critical density for excitation is $n_{cr} = 2 \times 10^5$ cm^{-3}) and N_2H^+ may deplete significantly only at densities $>10^5$ cm^{-3} (see Bergin & Langer 1997, Bergin et al. 2002). Only two of the five maxima of integrated line intensity found are coincident with peaks of millimeter continuum emission from dust. In addition, several peaks of dust emission are not coincident with maxima of integrated line intensity. This situation is different from that seen in isolated cores where coincidence between dust and N_2H^+ emission is common. The difference is likely due to variations in N_2H^+ abundance within Oph A arising from differences in the relative density and dust temperature within each object. Focusing on the line emission alone, we find that its widths vary by a factor of ∼5 in Oph A, with several locations having FWHMs < 0.3 km s^{-1}. The centroid velocities of the line emission vary little in Oph A, however, having an rms of only ∼0.17 km s^{-1}. Small-scale centroid velocity gradients are found near the SM1, SM1N, and SM2 objects. The quiescent and slow motions of objects in Oph A objects contrast sharply with the turblent and dynamic motions expected in some models of cluster formation. One integrated line intensity maximum, Oph A-N6, has line widths as low as 0.193 km s^{-1} FWHM, or just larger than the line width expected from thermal motions alone, indicating localized reduction of turbulent motions within Oph A.

Details of our observations are described in §2. We present the results in §3, including derivations of N_2H^+ column densities and H_2 column densities, and descriptions of the widths, centroids, and profiles of the N_2H^+ 1–0 line across Oph A. A discussion of the implications of our data is found in §4, and we summarize our conclusions in §5.

2. Observations

2.1. IRAM 30 m Telescope Observations

Observations of the Oph A core at the 93.17 GHz frequency of N_2H^+ 1–0, consisting of 7 hyperfine components over 4.6 MHz (see Caselli, Myers, & Thaddeus 1995; CMT95), were carried out with the IRAM 30 m telescope on Pico Veleta, Spain[2]. Data were obtained during three clear nights between 1998 June 25 and 1998 June 28, in association with a comprehensive molecular line study of the cores and condensations of the Ophiuchus protostellar cluster (Belloche et al. 2001; André et al. 2004, in preparation) Data were taken in the "on-the-fly" mapping mode (Ungerechts et al. 2000), with an individual dump time of 2 seconds, a scanning speed of $1''$ s^{-1}, and a spacing of $5''$ between consecutive scans. The reference position was taken at the location of the B3 star S1 (see Figure 1) which had previously been seen to be free of emission in any dense gas tracer such as N_2H^+ 1–0. The half-power beam width of the telescope was $\sim 26''$. An SIS heterodyne receiver was used with an autocorrelator as backend to give a spectral resolution of 19.5 kHz over 17.5 MHz. The corresponding spectral resolution was 0.06284 km s^{-1}.

The observations were done in single sideband mode, with a sideband rejection of 0.003 and an associated calibration uncertainty of $\sim$10%. The forward and beam efficiencies of the telescope used to convert antenna temperatures $T_{\rm A}^*$ into main beam temperatures $T_{\rm mb}$ were 92% and 73%, respectively. The system temperature ranged from $\sim$170 K to $\sim$200 K on the $T_{\rm A}^*$ scale. The telescope pointing was checked every $\sim$2 hours on the strong radio sources NRAO 530 or 1514-241 and found to be accurate to better than $\sim 5''$ (i.e, the maximum deviation between two consecutive pointings). The telescope focus, optimized on the same sources every $\sim$3-4 hours, was very stable. The data cube was produced and reduced with the CLASS software package (Buisson et al. 2002).

2.2. BIMA Millimeter Array Observations

The Oph A core was observed with the BIMA Millimeter Array located at Hat Creek, California, U.S.A.[3], over 2 tracks in its C-configuration (1999 May 04, 23) and 2 tracks in

[2]The Institut de RadioAstronomie Millimétrique (IRAM) is an international institute for research in millimeter astronomy, and is supported by the CNRS (Centre National de la Recherche Scientifique, France), the MPG (Max Planck Gesellschaft, Germany), and the IGN (Instituto Geografico Nacional, Spain).

[3]The BIMA array is operated with support from the U.S. National Science Foundation under grants AST-9981308 to the University of California, Berkeley, AST-9981363 to the University of Illinois, and AST-

its B-configuration (2000 March 14, 15). A total of 3 pointings was observed along the bright continuum filament associated with the A core detected by MAN98. The pointings were spaced by $\sim$1.′0, slightly less than required for Nyquist sampling, for a constant rms noise level along the filament. Each track consisted of cycled visits to the Oph A pointings interspersed with observations of radio sources 1625-254 (in 1999) or 1733-130 (in 2000) approximately every 20 minutes for phase calibration. Flux calibration was obtained from observations of 3C 273 and Neptune at the beginning and the end of each track respectively.

Data reduction was performed using standard tasks in the MIRIAD software package (see Sault, Teuben & Wright 1995). Quasar data were self-calibrated using fluxes bootstrapped from Neptune data, and the resulting amplitude and phase solutions were applied to the target pointings. All 3 pointings were inverted simultaneously, and the resulting mosaics were deconvolved with a cleaning algorithm based on that presented by Steer, Dewdney, & Ito (1984). The N_2H^+ 1–0 data were convolved with a Gaussian of 5.″0 × 0.″5 FWHM (P.A. = 90°) to improve the beam shape and increase brightness sensitivity. The final synthesized beam size was 9.″9 × 6.″1 FWHM (and P.A. = -13.18°), corresponding to a linear FWHM resolution of 0.0060 pc × 0.0037 pc at the 125 pc distance to Oph A.

2.3. Combining the Datasets

The BIMA and IRAM data of N_2H^+ 1–0 were combined to recover missing flux from extended structure resolved out in the interferometer map. The IRAM data were regridded in velocity from 0.06284 km s^{-1} channels to 0.07854 km s^{-1} channels to match the velocity resolution of the BIMA data. The MIRIAD task *immerge* was used for the combination, where the sum of the Fourier transforms of the clean BIMA and IRAM images is itself transformed into the image plane as the combined image. To ensure a common flux scale for the independent datasets prior to combination, visibilities of both were compared over 2–9 kλ, the maximum range of spatial frequencies in common, and a derived scaling factor of 1.11 was applied to the IRAM data. Comparing the total flux of the combined dataset convolved to a $\sim$27″ FWHM beam with that of the IRAM data, we estimate this method recovers 85% of the flux in the latter map over the region of interest.

9981289 to the University of Maryland.

3. Results

Figure 1a shows the 1.3 mm continuum emission from Oph A detected by MAN98 using the IRAM 30 m Telescope at 13″ FWHM resolution. Figure 1b shows the integrated intensity of N_2H^+ 1–0 line emission detected by us over the same region, using combined data from the IRAM 30 m Telescope and the BIMA millimeter interferometer at $\sim$10″ $\times$ $\sim$6″ FHWM resolution. The line emission from Oph A shows a filamentary structure similar to that shown by the continuum emission, although the width of the the integrated line emission structure is narrower than that of the continuum emission. Figure 1a shows positions of several objects in Oph A identified by MAN98 from their multiresolution wavelet analysis. Figure 1b shows these positions again as well as the positions of the various maxima of integrated intensity of N_2H^+ 1–0, which we have named here Oph A-N1 through N6 and whose positions are listed in Table 1. Some, but not complete, coincidence is seen between continuum objects and the maxima of integrated line intensity in Oph A. For example, SM1 and SM1N are coincident (within a beam FWHM) of N4 and N5 respectively (and possibly A-MM5 with N2 also). Some Oph A continuum objects, however, have little-to-no detected N_2H^+ 1–0 emission associated with them. For example, relatively little line emission is found at the positions of VLA 1623, SM2, A-MM6, A-MM7, and A-MM8. Furthermore, some maxima of the N_2H^+ 1–0 integrated intensity in Oph A, although coincident with extended continuum emission, are not associated with continuum objects. For example, N1, N3, and N6 are not associated with objects specifically identified by MAN98. The lack of coincidence between peaks of dust emission and maxima of N_2H^+ emission in Oph A is very different from the high level of coincidence between the two tracers seen in numerous isolated cores, albeit at lower resolution (e.g., Tafalla et al. 2002).

All 7 hyperfine components of the N_2H^+ 1–0 line from the combined data were fit simultaneously using the HFS (HyperFine Structure) fitting routine of the CLASS data analysis package (see Buisson et al.) For each 0.″75 $\times$ 0.″75 pixel of the data cube, these fits provided estimates of: 1) ΔV, the line FWHM, 2) V_{LSR}, the centroid velocity, 3) τ_{tot}, the sum of peak optical depths for all 7 hyperfine components, and 4) $(J_{ex}–J_{bg})\tau_{tot}$, the difference between the (Rayleigh-Jeans equivalent) excitation and background temperatures times τ_{tot}. (In the latter, $J_{ex} = (h\nu/k)/(\exp(h\nu/kT_{ex})\text{-}1)$, $J_{bg} = (h\nu/k)/(\exp(h\nu/kT_{bg})\text{-}1)$, and T_{ex} and T_{bg} are the actual excitation and background temperatures respectively.) The brightness temperature of the 1–0 line, T_B, can be estimated from

$$T_B = (J_{ex} - J_{bg})(1 - \exp(-\tau_{tot})). \quad (1)$$

Table 2 lists the mean, rms, minimum and maximum values of ΔV, V_{LSR}, T_B and τ_{tot} from

the combined data after averaging them into $10\farcs5 \times 6\farcs75$ pixels, i.e., pixels with areas slightly larger than those of the synthesized beam. Most notably, ΔV in Oph A varies widely but V_{LSR} does not. For example, ΔV varies by a factor of $\sim$5 in Oph A but the rms of V_{LSR} is only 0.17 km s^{-1}.

In the following, we describe the N_2H^+ data in more detail, using the results obtained by HFS fitting to examine the N_2H^+ column densities and abundances as well as the widths and centroid velocities of the N_2H^+ 1–0 line.

3.1. Column Densities and Abundances

Column densities of H_2, i.e., $N(H_2)$, can be determined in Oph A with the 1.3 mm continuum data of MAN98 (e.g., see Figure 1a) from

$$N(\mathrm{H_2}) = S_\nu/(\Omega_\mathrm{m}\mu m_H \kappa_\nu \mathrm{B}_\nu(T_{dust})), \tag{2}$$

where S_ν is the 1.3 mm flux density, Ω_m is the main-beam solid angle, μ is the mean molecular weight, m_H is the mass of atomic hydrogen, κ_ν is the dust opacity per unit mass at 1.3 mm (assumed to be 0.005 cm^2 g^{-1} for starless objects by MAN98; the local gas-to-dust ratio is assumed to be 100), and $\mathrm{B}_\nu(T_{dust})$ is the Planck function at T = T_{dust}.

Figure 2a shows $N(H_2)$ in Oph A obtained by assuming $T_{dust} = 20$ K at all locations (following MAN98). To facilitate comparision with the N_2H^+ data, the area shown is restricted to that where the peak brightness temperature of the brightest hyperfine component, $T_B^{max} \geq 3\,\sigma$ in the N_2H^+ 1–0 line data. Furthermore, the MAN98 continuum data were binned into pixels $10\farcs5 \times 6\farcs75$ in size using standard image interpolation methods in MIRIAD to obtain pixels with areas approximately that of the beam of the N_2H^+ observations. (Note that each pixel in Figure 2a is still not spatially independent of its neighbors.) Figure 2a shows the $N(H_2)$ distribution across Oph A is similar to that of the 1.3 mm continuum emission shown in Figure 1a, due of course to the linear proportionality between the two quantities in Equation 2 if T_{dust} is constant. Table 3 lists the mean, rms, minimum, and maximum of $N(H_2)$ shown in Figure 2a.

Column densities of N_2H^+, i.e., $N(N_2H^+)$, can be determined along the Oph A filament from the line characteristics obtained from HFS fitting (see §3). Assuming LTE, i.e., all level populations are described by a single excitation temperature, T_{ex}, $N(N_2H^+)$ can be found following Womack, Ziurys, & Wyckoff (1992) from

$$N(\mathrm{N_2H^+}) \approx \frac{1}{1.06(J+1)} \frac{3h}{8\pi^3 \mu_e^2} \frac{k}{hB} \left(T_{ex} + \frac{hB}{3k} \right) \frac{e^{E_J/kT_{ex}}}{(1 - e^{-h\nu/kT_{ex}})} \Delta V \tau_{tot}, \quad (3)$$

where ΔV and τ_{tot} are found from HFS fits to data averaged to $10\farcs5 \times 6\farcs75$ pixels. In addition, J is the lower rotational level number (i.e., 0), μ_e is the dipole moment of the N_2H^+ molecular ion (i.e., 3.40 Debye; Green, Montgomery & Thaddeus 1974), B is the rotational constant of N_2H^+ (i.e., 46.586702 GHz; see CMT95) and E_J is the energy above ground of the lower rotational level (i.e., 0).

Figure 2b shows $N(N_2H^+)$ in Oph A obtained using the results of our HFS fits and Equation 3.[4] Figure 2b shows the $N(N_2H^+)$ distribution across Oph A is not similar to the $N(H_2)$ distribution, but rather is similar to that of the N_2H^+ integrated intensities shown in Figure 1b. Table 3 lists the mean, rms, minimum, and maximum of $N(N_2H^+)$ shown in Figure 2b. We note that assuming LTE in Oph A can result in overestimates of $N(N_2H^+)$ from N_2H^+ 1–0 emission toward locations with densities $< 10^6$ cm^{-3} (e.g., by factors of $\sim$2 where densities are $\sim 10^4$ cm^{-3}; E. Bergin, private communication.) As discussed in §4.1, however, mean densities are $>10^6$ cm^{-3} towards positions of bright N_2H^+ 1–0 emission in Oph A.

Figure 2c shows the N_2H^+ fractional abundance across Oph A, determined using values from Figures 3a and 3b (i.e., $X(N_2H^+) = N(N_2H^+)/N(H_2)$). The mean $X(N_2H^+)$ derived, 1.9×10^{-10}, is similar to values derived for other dark clouds, e.g., $X(N_2H^+) \approx 10^{-10}$ has been found in various cores by Caselli et al. (2002a), Tafalla et al. (2002), Benson, Caselli, & Myers (1998), Womack et al. (1992), and Ohishi, Irvine, & Kaifu (1992). Within Oph A itself, Figure 2c shows that $X(N_2H^+)$ varies by a factor of $\sim$40, with lower values at the edges of the filament and near the continuum objects like SM2, and higher values at positions at the extreme northern and southern ends of the filament. Table 3 lists the mean, rms, minimum, and maximum of $X(N_2H^+)$ shown in Figure 2c.

Assuming LTE, our accuracy in determining $X(N_2H^+)$ is limited by our knowledge of T_{dust} within Oph A[5]. Indeed, isothermal dust is arguably not expected in Oph A given the

[4]Using Equation 3, $\sim$80% of beam-sized pixels had derived values of T_{ex} between 6 K and 24 K with a peak at $\sim$15 K, but the remaining $\sim$20% had values extending up to 260 K. These latter values were found typically if $\tau_{tot} < 0.2$; high values of T_{ex} are obtained in such cases because only the product of J_{ex} and τ_{tot} is constrained. In these instances, the derived T_{ex} values were deemed spurious, and $N(N_2H^+)$ values were calculated using Equation 3 after substituting T_B for the factor $(T_{ex} + hB/3k)\tau_{tot}$ and assuming in the exponential factors $T_{ex} = 14.9$ K, the mean T_{ex} of the other $\sim$80% of pixels.

[5]In addition, dust mass opacities, κ_ν, may vary in Oph A by factors of $\sim$2 or more due to grain evolution

number of nearby heating sources (i.e., embedded cluster members) and the wide range of column densities (i.e., extinctions) present. For the continuum objects, dust temperatures determined independently can be used to determine more refined, specific values of $X(N_2H^+)$. Table 4 lists values of T_{dust} for continuum objects in Oph A by AWB93, determined by modeling their submillimeter spectral energy distributions. (AWB93 found dust emissivities of $\kappa_\nu \propto \nu^{1.5}$, i.e., $\kappa_{1.3mm} \approx 0.01$ cm^2 g^{-1}, best fit their data.) AWB93 speculated these differences may be due to radiative heating by nearby sources to the northeast of SM1, e.g., the nearby B3 star S1. Table 4 also lists values of $X(N_2H^+)$, $N(N_2H^+)$, and $N(H_2)$ for VLA 1623, SM1N, SM1, and SM2 obtained by assuming the T_{dust} values of AWB93 in Equations 2 and 3 and averaging the resulting values over 3-4 beam-sized pixels coincident with each object. (For VLA 1623, upper limits for $N(N_2H^+)$ and $X(N_2H^+)$ are given in Table 4 since it is located where $T_B^{max} < 3\ \sigma$.) The difference in $X(N_2H^+)$ from one source to the next is smaller when constant T_{dust} is used. N_2H^+ abundances are similar for SM1N and SM1 while those of SM2 and VLA 1623 are lower by factors >4. (Oph A-N6, also in Table 4, will be discussed in §3.2.)

For locations in Oph A beyond the continuum objects, specific values of T_{dust} have not been defined, e.g., AWB93 did not derive T_{dust} values there. Maps of submillimeter continuum spectral indicies by AWB93, however, indicate that a T_{dust} gradient exists across Oph A, with lower T_{dust} (i.e., $\leq$ 15 K) to the south or southwest (near VLA 1623 and SM2) and higher T_{dust} (i.e., $\geq$ 25 K) to the north or northeast (near SM1 and SM1N). Unfortunately, the AWB93 submillimeter (e.g., 350 μm) continuum maps do not cover well the extreme northern and southern ends of the filament where we find the highest values of $X(N_2H^+)$, i.e., assuming $T_{dust} = 20$ K. Without specific estimates for T_{dust}, it is difficult to refine our estimates of $X(N_2H^+)$ at the ends of the filament. We note, however, that $X(N_2H^+)$ at these locations would be quite similar to those of SM1 and SM1N if $T_{dust} \approx$ 10–12 K, quite significantly reducing the abundance contrast shown by Figure 2c. At the very least, our observations suggest differences in $X(N_2H^+)$ for the continuum objects in Oph A by factors $\geq$4. Put simply, variations of both $X(N_2H^+)$ and T_{dust} appear necessary to reconcile the 1.3 mm continuum and N_2H^+ line data of Oph A.

(see MAN98 and references therein). In this paper, we assume constant κ_ν since we are considering similar objects where differences in dust opacities are likely minimal.

3.2. Line Widths

Figure 3a shows a map of ΔV obtained from the HFS fits of the combined N_2H^+ data of Oph A. The data shown are only those where $T_B^{max} \geq 3\ \sigma$. The large variation of ΔV in Oph A by a factor of $\sim$5 differs from the relatively little variation of line widths (i.e., "coherence") found over similar $\sim$0.1 pc length scales in isolated, quiescent cores by Goodman et al. (1998). Table 4 lists the ΔV of SM1N, SM1, and SM2, obtained by averaging over 4 beam-sized pixels surrounding each object. These continuum objects are coincident with locations in Oph A with relatively broad N_2H^+ lines, i.e., $\Delta V \approx 0.5$–0.6 km s^{-1}. We note also that the largest line widths are found adjacent to (but not coincident with) these continuum objects.

Figure 3a shows fourteen locations in Oph A with $\Delta V \leq 0.30$ km s^{-1}, which we arbitrarily define as "very narrow." Table 5 lists these positions, named here as locations "a" through "n", and gives their mean line width within the 0.3 km s^{-1} contour. No very narrow line width location is coincident with an identified continuum object, although location "c", near A-MM5, may be an exception. Eleven very narrow line width locations are at the edges of the detected filament, where line peaks are relatively weak and near our detection limit (i.e., $T_B^{max} \approx 3\ \sigma$) and where HFS fits are relatively poor (e.g., typical ΔV uncertainties are $\sim$0.02-0.05 km s^{-1}.) Conversely, only the "b", "f, and "l" locations are well-defined local minima of ΔV; each is surrounded by larger ΔV and has line peaks well above our detection limit (e.g., typical ΔV uncertainties are $\sim$0.005-0.01 km s^{-1}). The extents of most very narrow line locations are therefore not well defined spatially since narrow line emission below our detection limit may or may not reside adjacent to each. Finally, most narrow line locations have detected extents smaller than the beam. Only the "c", "d", "l", and "m" locations have detected extents larger than the beam.

The very narrow line location "l" is especially notable in Oph A given its resolved extent, the relative brightness and the narrowness of its N_2H^+ 1–0 line emission, and its association with a maximum of integrated intensity (i.e., Oph A-N6). The "b" and "f" locations are like "l" in that they are also associated with bright emission (i.e., Oph A-N1), but unlike "l" they are each spatially unresolved and their lines are slightly broader than those of "l". The "c", "d", and "m" locations are like "l" in that they are each spatially resolved and their lines are similarly as narrow than those of "l" (or less), but unlike "l" they are not spatially well-defined and have weaker emission (i.e., no associations with integrated intensity maxima). These limitations make the "b", "c", "d", "f", and "m" locations more difficult to characterize than "l", so we concentrate on "l" in the following discussion. (The conclusions we reach on "l" may also apply to these other very narrow line positions.) Since "l" includes Oph A-N6 we henceforth refer to this "object" or location within Oph A simply as Oph A-N6

or N6 for short. Table 4 lists values of $X(N_2H^+)$, etc., for N6 found by averaging values over 5 beam-sized pixels coincident with positions where $\Delta V \leq 0.30$ km s^{-1}, and assuming $T_{dust} = 15$ K at that location (see §3.1). Although the position of minimum line width in N6 is $\sim$19″ from its position of maximum integrated intensity, line emission is quite narrow throughout N6; when averaged over 5 adjacent beam-sized pixels, the ΔV of N6 is 0.25 km s^{-1} (see Table 4).

The minimum line width in Oph A-N6 is remarkably small, only 0.193 ± 0.008 km s^{-1}. Figure 4 shows the spectrum of N_2H^+ 1–0 at the location of minimum line width in Oph A-N6, along with its HFS fit. All 7 hyperfine components of N_2H^+ 1–0 are unblended and clearly discernable at this position. Given the finite 0.07854 km s^{-1} velocity resolution, the actual line widths are slightly less than the values shown in Figure 3a, depending on the line width. For example, the minimum ΔV in Oph A-N6 reduces to only 0.176 km s^{-1} when the velocity resolution is subtracted in quadrature. Such narrow line widths are actually comparable to the thermal FWHMs expected for N_2H^+ given expected gas temperatures, T_{gas}, within Oph A. For example, Wootten et al. (2004, in preparation) using VLA NH_3 data have determined gas temperatures for the Oph A continuum objects that are similar to the $T = 20$ K assumed by MAN98, i.e., 16 K for SM1, 21 K for SM1N, and 18 K for SM2. Other estimates of T_{gas} in Oph A can be made using the values of T_{ex} found from HFS fits of the N_2H^+ 1–0 line at positions where $\tau_{tot} >> 1$, assuming the transition is thermalized, i.e., the local density is well above its 2×10^5 cm^{-3} critical density. (Below we show that this is reasonable within Oph A-N6, given its size and mass.) For the minimum ΔV spectrum shown in Figure 4, values of $T_{ex} = 18.1$ K $\pm$ 3.4 K and $\tau_{tot} = 12.0 \pm 2.2$ were found, suggesting $T_{gas} \approx 18$ K. Within Oph A-N6 where $\tau_{tot} \geq 11.57$ (i.e., where the optical depth of the brightest hyperfine component, 123-012, is at least 3), the mean T_{ex} is 17.4 K. If $T_{gas} = 18.1$ K at the position of the spectrum shown in Figure 4, the expected thermal FHWM is 0.169 km s^{-1}. The FWHM of the nonthermal component to ΔV at this position, ΔV_{NT}, obtained by subtracting in quadrature the thermal FWHM, ΔV_T, from the resolution-corrected FWHM, is only 0.0500 km s^{-1}. Although the spectrum shown in Figure 4 is the narrowest in Oph A-N6, the gas velocities there are all remarkably dominated by thermal motions, with relatively little nonthermal contributions.

The occurrence of near-thermal line widths in Oph A is significant because the Ophiuchus star-forming clouds are turbulent on larger spatial scales and at lower densities (see Loren 1989a). Near-thermal line widths have been observed previously towards isolated cores; e.g., see Jijina, Myers, & Adams (1999) for a detailed list based on NH_3 observations and Benson et al. (1998) and Caselli et al. (2002a) for N_2H^+ observations. Oph A-N6 is similar to the quiescent regions in Serpens NW identified using N_2H^+ 1–0 by Williams & Myers (2000). For example, the average ΔV_{NT} for Oph A-N6, assuming $T_{gas} = 18$ K, is

0.17 km s^{-1}, similar to objects at the lower end of the ΔV_{NT} range reported by Williams & Myers. There are, however, some important differences between Oph A-N6 and the quiescent Serpens objects. For example, the minimum ΔV_{NT} of Oph A-N6 is smaller than those reported for the Serpens objects by a factor of $\sim$3. Furthermore, Oph A-N6 contains an obvious maximum of N_2H^+ 1–0 integrated intensity, whereas the Serpens objects are not. Other instances of N_2H^+ 1–0 as narrow as 0.2 km s^{-1} were detected within NGC 1333 IRAS 4 by Di Francesco et al. 2001 (see also Walsh et al. 2004, in preparation, for other locations in NGC 1333.) In contrast to Oph A-N6, ΔV_{NT} = 0.46-0.57 km s^{-1} for SM1N, SM1, and SM2, given their respective values of ΔV listed in Table 4 and the T_{gas} values found by Wootten et al.

Within Ophiuchus, extremely narrow lines such as those described here have been uncommonly observed, possibly due to the relatively large beam sizes of earlier studies. For example, Loren (1989b) found ΔV = 1.7 km s^{-1} for ^{13}CO 1–0 in the general Oph A region (R22) when observed with a 2.4′ beam (although the line was considered saturated.) In addition, Tachihara, Mizuno, & Fukui (2000) found ΔV = 1.5 km s^{-1} for the C^{18}O 1–0 core in the neighbourhood of Oph A (ρ Oph 2). Furthermore, LWW90 found ΔV = 0.8 km s^{-1} and 0.7 km s^{-1} for DCO^+ 3–2 at the "core center" of Oph A (defined then as $\sim$10″ west of SM1N) when observed with a 1.′2 FWHM beam and a 0.′5 FWHM beam respectively. Belloche et al. (2001), however, detected relatively narrow N_2H^+ 1–0 lines at various locations within Oph, e.g., ΔV = 0.26 km s^{-1} toward Oph E-MM2, in IRAM 30 m Telescope data alone (obtained with a 0.′45 FWHM beam.) Our IRAM 30 m Telescope data is a subset of the Belloche et al. data and across Oph A-N6 they show no evidence of the narrower lines seen in the combined data, i.e, ΔV = 0.35 km s^{-1}. Our high angular resolution data have revealed locations of extremely narrow line emission in Oph A.

3.3. Line Centroids and Profiles

Figure 3b shows a map of V_{LSR}, the central velocity of the N_2H^+ 1–0 line, in Oph A obtained from HFS fits to the combined data. Immediately striking in this Figure is the narrow range of V_{LSR} values within Oph A; the rms of V_{LSR} values is only 0.17 km s^{-1} (see Table 1). Figure 3b reveals no large-scale gradient of V_{LSR} along Oph A but small-scale gradients are possibly found near the continuum objects SM1N, SM1, and SM2, roughly aligned east-west or west-east. Other possible gradients include one north of VLA 1623 aligned north-south, and one northwest of SM1N (and Oph A-N1) aligned northwest-southeast. In contrast, no V_{LSR} gradient is found toward Oph A-N6. (As noted earlier, weak emission in its periphery are at slightly lower V_{LSR}.)

Figure 5 shows a spectral grid of N_2H^+ 101–012, the "isolated component" of N_2H^+ across Oph A, where each panel shows the line averaged over a (beam-sized) $10\farcs5 \times 6\farcs75$ area. The variation of ΔV and lack of variation of V_{LSR} across Oph A are easily apparent in this Figure, but the line shapes are more evident here than possible from maps of HFS fit parameters. Figure 5 reveals that the N_2H^+ line profiles in Oph A are typically symmetric in most locations, with little evidence for self-reversal or asymmetry. This appearance is consistent with the relatively low optical depths of the lines here as obtained from HFS fits (see Figure 2b). Only at a position just west of SM1 is a single self-reversal found, and perhaps not coincidentally this location is also that of maximum $N(N_2H^+)$ in Oph A as derived from the HFS fits. The line shapes reveal little evidence for the asymmetrically-blue line profiles that suggest infall motions, such as those seen in N_2H^+ 1–0 towards L1544 by Williams et al. (1998), likely also due to the relatively low optical depths of the line in Oph A. Only one possible instance of blue asymmetry is found in Oph A, immediately southwest of SM1. This spectrum, however, is adjacent to an instance of red asymmetry, and both asymmetries may be consistent with having been made from noise across the line. The line shapes also show no evidence for broad line wings expected from high velocity outflows.

Surprisingly, the line velocities of N_2H^+ 1–0 appear correlated with its line width, but only for the brightest lines in Oph A, i.e. towards the highest N_2H^+ column densities. Figure 6a shows that higher velocity (redder) lines are systematically wider in lines where $T_B^{max} \geq 10\,\sigma$. A linear fit to the data shown in Figure 6a reveals a fairly high correlation parameter r of 0.82 (see Press et al. 1992). Figure 6b shows, however, that a similar correlation between V_{LSR} and ΔV is less likely for lines with $T_B^{max} < 10\,\sigma$; the r obtained from a linear fit to this subsample is only 0.31. Figure 7 shows evidence that the line widths are increasing because only their red sides are moving to higher velocities and their blue sides are not shifting in velocity. Three pairs of 2 spectra of the N_2H^+ 101-012 line are shown, taken from different positions in Oph A, where each pair consists of an average over 2-4 neighboring pixels with bright narrow emission in Oph A and an average over 4-6 surrounding pixels with fainter, broader emission. This Figure suggests that the trend shown in Figure 6a is not simply a matter of the widths of bright lines increasing as the entire line shifts to higher velocities. A similar trend is suggested by N_2H^+ 1–0 line data of the quiescent region Q8 of Serpens (Williams & Myers) and NGC 1333 IRAS 4B in Perseus (Di Francesco et al.)

4. Discussion

Our combined single-dish and interferometer data have revealed interesting variations of N_2H^+ abundance and the width and centroid velocity of the N_2H^+ 1–0 line within the Oph A

filament. Together, these variations provide a qualitative picture of the protostellar evolution of gas and dust in a relatively dense star-forming core, assuming that the differences are due solely to evolution. In this picture, the "object" Oph A-N6 represents a relatively early, quiescent stage marked by high density, low T_{dust}, high $X(N_2H^+)$, low ΔV, and little local variation of V_{LSR}. SM2, however, represents a more-evolved protostellar stage with higher density, low T_{dust}, low $X(N_2H^+)$, medium ΔV, and some local variation of V_{LSR}. SM1N and SM1 may be at a similar protostellar stage as SM2 given their similar ΔV and variation of V_{LSR}, but their higher $X(N_2H^+)$ may reflect their higher T_{dust}. Finally, VLA 1623, which has just formed a protostar (AWB93), is representative of the next stage of evolution, namely the beginning of the protostellar phase. It has high density, low T_{dust}, and very low $X(N_2H^+)$. In the following, we describe in more detail how the differences in $X(N_2H^+)$, ΔV, and V_{LSR} between the Oph A objects result in this qualitative picture.

4.1. N_2H^+ Abundances

Variations of N_2H^+ abundance in Oph A point to subtle differences in the evolutionary stages of its starless objects due to the expected behavior of $X(N_2H^+)$ within cold, dense environments. Although $X(N_2H^+)$ can be reduced locally as a result of outflows, e.g., when H_2O and CO are returned to the gas phase by shocks and quickly deplete N_2H^+ via ion-molecule reactions (see Bergin, Neufeld, & Melnick 1998; van Dishoeck & Hogerheijde 1999), these objects do not contain or are not impacted by any outflowing gas (Kamazaki et al. 2001, 2003). Lee et al. (2003) have suggested molecular abundance differences between starless objects can be related also to the relative ratio of their dynamical and chemical time scales (i.e., their respective environments), but the Oph A objects should have this factor in common since they are situated within the same core[6]. Gas-grain chemistry at high densities and low temperatures is a very plausible cause of these variations.

Examples of the effect of gas-grain chemistry on $X(N_2H^+)$ in cold, dense environments were recently provided by Aikawa, Ohashi, & Herbst (2003; AOH03). AOH03 found from isothermal (i.e., $T_K = 10$ K) models of Larson-Penston collapsing starless objects that central $X(N_2H^+)$ increases when central densities increase up to $\sim 3 \times 10^6$ cm^{-3} (e.g., that expected for L1544), as the principal destroyers of N_2H^+ like CO become strongly depleted onto dust grains (see also Bergin & Langer, Shematovich et al. 2003). At densities $\approx 3 \times 10^7$ cm^{-3}, however, AOH03 found that $X(N_2H^+)$ *decreases* by a factor of $\sim$2 from its maximum within

[6]Again, variations in grain size distribution may be relevant to abundance differences but we have assumed constant κ_ν throughout Oph A.

a ∼1000 AU radius as N_2, from which N_2H^+ forms, is adsorbed onto dust grains. Although not explored explicitly by AOH03, further N_2H^+ depletion may be expected at still higher central densities. Observational evidence for central N_2H^+ depletions have been reported recently in isolated starless objects with central densities of $\sim 10^{5-6}$ cm^{-3}, e.g., B68 (Bergin et al.), L1544 (Caselli et al. 2003), and IRAM 04191+1522 (Belloche & Andre 2004, in preparation).

The models of AOH03 imply that depletion of N_2H^+ can be hard to observe directly with large beams. For example, no central minimum in $N(N_2H^+)$ can be seen when their model core is "observed" with a beam of ∼4000 AU equivalent FWHM (see their Figure 9). Given their small extent, such N_2H^+ depletion zones would be easier to detect directly with smaller beams. For example, our combined N_2H^+ data have a geometrical mean linear resolution of 970 AU at the 125 pc distance of Oph A, or about half the diameter of the central N_2H^+ depletion zone in the AOH03 models. The variations of $X(N_2H^+)$ between the Oph A objects we observe could be then explained as the result of detecting differing amounts of depletion due to density differences between objects. MAN98 determined mean densities for SM1N, SM1, and SM2 from their 1.3 mm continuum observations ranging from $\sim 5 \times 10^6$ cm^{-3} (SM2) to $\sim 4 \times 10^7$ cm^{-3} (SM1N), i.e., in the regime where central N_2H^+ depletions were found by AOH03. Note, however, that the AOH03 models had constant $T_K = 10$ K, so the possible effect on depletion that warmer T_{dust} may have must also be considered in an intepretation.

Table 4 lists $X(N_2H^+)$, $N(N_2H^+)$, and $N(H_2)$ for Oph A-N6 in addition to those for VLA 1623, SM1N, SM1, and SM2, also found using Equations 2 and 3 and averaging over coincident beam-sized pixels. For N6, we assume $T_{dust} = 15$ K following AWB93, although they suggested that $T_{dust} \leq 15$ K southeast of SM2. The $N(N_2H^+)$ of N6, 6×10^{13} cm^{-2}, lies between the higher values of SM1 and SM1N and the lower values of SM2 and VLA 1623. On the other hand, the $N(H_2)$ of N6, $\sim 3 \times 10^{23}$ cm^{-2}, is actually similar to those of SM1N and SM1, but appears smaller than those of VLA 1623 and SM2.

Relative to Oph A-N6, VLA 1623 and SM2 have likely higher mean densities, given their apparently larger $N(H_2)$ and more compact appearance as 1.3 mm continuum maxima. In the context of the AOH03 models, their low N_2H^+ column densities are due to N_2H^+ depletion at high density. Since VLA 1623 has formed a protostar (or two; see Looney, Mundy, & Welch 2000) but SM2 not formed any, the mean density of VLA 1623 should be even larger than that of SM2. The weaker N_2H^+ emission of VLA 1623 compared to SM2 likely reflects even greater N_2H^+ depletion that should accompany higher density. (In addition, N_2H^+ depletion toward VLA 1623 may be enhanced if grain mantles containing CO have returned to the gas phase through evaporation or outflow shocks.) SM1N and SM1 do

not fit easily into this sequence, however, as they have higher $N(N_2H^+)$ but similar $N(H_2)$. Their higher $N(N_2H^+)$ may reflect their warmer T_{dust} relative to SM2 if N_2 does not easily adsorb onto their warmer dust grains. CO, however, is likely also not adsorbed readily at these T_{dust} values, and its presence in the gas phase likely would reduce $N(N_2H^+)$ rather than increase it. The relatively high $N(N_2H^+)$ for SM1N and SM1 may be due to internal, dense regions where CO has been depleted but not N_2, i.e., that are cooler than suggested by their (average) T_{dust} but warmer than regions of similar density in SM2.

Since density must increase as a result of evolution towards star formation and $X(N_2H^+)$ appears to decrease above $\sim 10^6$ cm^{-3}, $X(N_2H^+)$ may be useful as an indicator of the relative evolution of several objects forming within the same dense core. Our $X(N_2H^+)$ results alone therefore suggest that Oph A-N6 is at an earlier stage relative to SM2 and that SM2 is at an earlier stage relative to VLA 1623. Given the warmer T_{dust} of SM1N and SM1 relative to SM2, their evolutionary stage relative to N6, SM2, and VLA 1623 is difficult to judge. We stress that these results are highly qualitative. Evans et al. (2001) and Zucconi, Walmsley, & Galli (2001) have shown recently that Bonnor-Ebert spheres with radial temperature gradients (e.g., with low central T_{dust}) are better than isothermal models in reproducing the observed dust emission of isolated starless objects, and the T_{dust} values derived by AWB93 and used here are likely averages of the actual dust temperature distributions within the Oph A objects. More detailed modeling of the dust continuum emission of all these objects is clearly required to determine better their thermal and density structures and provide more quantitative results, especially if N_2 depletion onto dust grains is strongly dependent on T_{dust}.

4.2. Nonthermal Motions and Velocity Gradients

Variations of the ΔV and V_{LSR} of N_2H^+ 1–0 in Oph A allow us to probe the dynamics of dense gas within the core. Complementing the previous discussion on N_2H^+ abundances, the dynamics of dense gas provide further insight into the relative evolution of objects within Oph A. In the following, we consider separately the dynamics of Oph A as a whole and of its population of starless objects, as well as those of Oph A-N6 relative to SM1N, SM1, and SM2.

4.2.1. The Oph A Core

The effective average velocity dispersion of gas, σ, within Oph A can be estimated from our data and compared to simple models to evaluate the dynamical state of the core. Following Bertoldi & McKee (1992; Appendix C), σ can be estimated in several ways. First, the dispersion of an average spectrum comprised of all line data across the core can be measured and σ^2 is approximately equal to the quadrature sum of this quantity and the thermal dispersion, i.e., that of velocities of mean molecular mass expected from thermal motions. The FWHM resulting from a Gaussian fit to such an average spectrum from our Oph A data is 0.58 km s^{-1}, yielding $\sigma = 0.36$ km s^{-1} if $T_K = 20$ K. Second, the rms of both ΔV and V_{LSR} can be measured and σ^2 is approximately equal to the sum of the squares of these quantities and the thermal dispersion. Using values from Table 1 and again assuming $T_K = 20$ K, $\sigma = 0.33$ km s^{-1}, i.e., within 10% of the first value.

The estimated σ of Oph A is similar to but less than expected from simple virial arguments, i.e., those that ignore contributions from surface pressure and magnetic fields[7]. For example, the average total one-dimensional velocity dispersion of a virialized core can be estimated by equating $2T = 2(3/2)M\sigma^2$, the magnitude of the total core kinetic energy (M is the total core mass), and $W = (3/5R)aGM^2$, the magnitude of the total core gravitational potential energy (R_m is the average projected core size, G is the gravitational constant, and a is a dimensionless parameter accounting for core asphericity and nonuniformity; see Bertoldi & McKee). For Oph A, $M \approx 11$ M$_\odot$, assuming $T_{dust} = 20$ K on average and using the 1.3 mm continuum data of MAN98 over positions with detected N_2H^+ 1–0 emission. We find $\sigma = 0.57$ km s^{-1}, assuming this mass and uniformity in density. (An aspect ratio of $\sim$7 and a projected semiminor axis of $\sim$0.01 pc are also assumed, yielding $R_m = 0.023$ pc and $a = 0.78$; see Fig. 2 of Bertoldi & McKee.) These velocities suggest Oph A as a whole is in gravitational virial equilibrium to first order, i.e., they are within a factor of 2 of those required. (Although these velocities suggest Oph A has insufficient support against gravity in the absence of significant magnetic energy, the difference is likely not significant given the uncertainties in our analysis.) AWB93 also concluded the Oph A filament was similarly close to gravitational virial equilibrium, based on their submillimeter continuum data and a typical ΔV from available line data. More recently, Tachihara et al. found similar conclusions for (lower density) star forming C^{18}O cores in the near-neighborhood of Oph A. Better determinations of the local magnetic field strengths are clearly needed to evaluate better the global dynamical state of Oph A.

---

[7]Significant surface pressure would increase this dispersion but significant magnetic field energy would decrease it. Within Ophiuchus, however, magnetic field strengths appear small; e.g., $B_\parallel \leq 10$ μG was found in Oph from OH Zeeman measurements by Troland et al. (1996).

4.2.2. The Starless Object Population

Variations of V_{LSR} in the population of objects within Oph A provide constraints on some models of clustered star formation. Table 4 lists the V_{LSR} of SM1N, SM1, SM2, and Oph A-N6, obtained by averaging 4-5 beam-sized pixels around each object. The rms of these values is only 0.10 km s^{-1}, or $\sim$0.4 c_s(20 K), the isothermal sound speed of molecular gas at T_{gas} = 20 K. The similarities between the V_{LSR} of gas associated with the continuum objects and Oph A-N6 suggest strongly that all these lie within the same filament, and are not objects in separate cores seen by coincidence near each other towards Ophiuchus. Furthermore, the objects do not have substantial radial velocities relative to their neighboring dense gas. For example, the mean difference in the V_{LSR} of a given Oph A object and the mean of its surrounding gas is only 0.06 km s^{-1}, much smaller than the rms of V_{LSR}. This value is only $\sim$0.25 c_s(20 K), i.e., at the low end of expected mean relative gas velocities in cluster formation models where starless objects move ballistically within a core and accrete mass competitively (e.g., see Bonnell et al. 1997, 2001). The Oph A objects, however, are few in number, are found in close proximity, and as a whole may be at a relatively early, slow stage of such an evolution (e.g., when gas dominates the gravitational potential).

4.2.3. Oph A-N6

Variations of ΔV between starless objects in Oph A may be also related to these objects being at different stages in the evolution of dense gas towards star formation. Here we consider Oph A-N6 as an object, to place its physical characteristics in the context of models relevant to these epochs. Unlike SM1, SM1N, and SM2, N6 is not a local 2D maximum of continuum emission (i.e., $N(H_2)$), but instead resides on a gradient of continuum emission along the local northwest-southeast direction of the filamentary N_2H^+ 1–0 emission. Note, however, that N6 is at least at a 1D maximum of continuum emission in the direction perpendicular to the filament.

Given its 125 pc distance and following our arbitrary definition of its extent, i.e., where $\Delta V \leq$ 0.30 km s^{-1}, Oph A-N6 has a (nondeconvolved) geometrical mean radius of 0.008 pc. From its 1.3 mm continuum emission (see Fig. 1a) and assuming its dust is isothermal at T_{dust} = 15 K, N6 has a mean column density of 2.5 $\times$ 10^{23} cm^{-2} and a mass of 0.9 M$_\odot$. (Assuming N6 is a sphere, its mean density is 7.6 $\times$ 10^6 cm^{-2}, well above the 2.5 $\times$ 10^5 critical density of the N_2H^+ 1–0 line.) In addition, N6 has a mean ΔV = 0.25 km s^{-1} (see Table 4), suggesting a mean dispersion for the N_2H^+ 1–0 line of 0.11 km s^{-1}. Assuming the gas of N6 is isothermal at T_{gas} = 17.4 K (see §3), the mean nonthermal component σ_{NT} = 0.080 km s^{-1} and σ = 0.26 km s^{-1}.

The observed quantities of Oph A-N6 are within a factor of 2 of those predicted from simple models of equilibrium spheres. For example, the mass-radius ratio of a uniform sphere in gravitational virial equilibrium is $5\sigma^2/G$ and that of a critically-stable Bonnor-Ebert sphere is $2.4\sigma^2/G$ (Bonnor 1956). Given the effective radius and mass of N6, the mean velocity dispersions predicted from these simple models are 0.31 km s^{-1} and 0.45 km s^{-1} respectively, i.e., more than that of N6 itself by factors of 1.2 and 1.7 respectively. Like Oph A as a whole, N6 is in gravitational virial equilibrium to first order. (Again, the differences are likely not significant enough to suggest N6 has insufficent support against gravity.) Interestingly, the mass and radius of N6 can be reproduced simultaneously if the mass-radius ratio $\approx 7\sigma^2/G$, a situation that could occur, e.g., in virial equilibrium if magnetic energy $B \approx (6/5)M\sigma^2$, or more if surface pressure is also non-zero.

There are three questions about Oph A-N6 that simple equilibrium models do not directly address. First, why does N6 have such narrow line widths that suggest it has relatively little turbulence? Second, why are these line widths narrower than those in its immediate surroundings? Third, why is N6 located so close to its neighbor SM2? These questions may be answered simultaneously by considering models of equilibrium spheres embedded in sufficiently turbulent and opaque cores. Within such environments, turbulent motions could be reduced locally, e.g., if the spheres were similar or smaller in size than the cutoff wavelength for MHD waves in their surroundings (McKee 1989, McKee et al. 1993). (Turbulence could instead be damped locally by other processes such as shocks or dissipation; e.g., see Nakano 1998.) Myers (1999; see also Myers 1997), following reasoning by Larson (1985) and Mouschovias (1991), proposed thermally dominated, critically stable Bonnor-Ebert spheres could exist within turbulent, opaque, and dense cores. Such cores require large column densities (e.g., $A_V > 4$), so that ionization by cosmic rays dominates over that by ultraviolet radiation, and the coupling between the magnetic field and the gas is minimized. The embedded objects, called "kernels" by Myers, would be compressed by external (turbulent) core pressure to sizes comparable to the observed separations of young stellar objects within embedded clusters (e.g., ∼0.05-0.15 pc). A protostellar cluster could then arise from the near-simultaneous collapse of several kernels within a common core.

Oph A-N6 may be an excellent candidate for a kernel-like object, given its near-thermal line widths. Furthermore, its 0.9 $M_\odot$ mass matches quite well the 0.8 $M_\odot$ mean mass predicted for kernels within nearby star forming molecular cores, i.e., masses obtained by Myers using values of T, ΔV_{NT} and n derived by from Harju, Walmsley, & Wouterloot (1993) and Ladd, Myers, & Goodman (1994). Also, the projected separation between N6 and SM2 is 0.025 pc, within a factor of ∼2 of the ∼0.05 pc separation of kernels predicted by Myers. (Indeed, the mean nearest-neighbor separation of N6, SM1N, SM1, SM2, and VLA 1623, is only 0.023 pc.) Oph A-N6 does not fit completely to a kernel interpretation, however. As

noted above, its 0.008 pc radius is ∼3 smaller than the 0.024 pc mean radius expected for such kernels. (Note that the radius of a singular isothermal sphere (Shu 1977) at $T = 17.4$ K required to make a 0.9 $M_\odot$ star is ∼0.032 pc, a factor of ∼4 larger than that of N6.) Despite these caveats, however, the kernel model provides at least some basis for understanding N6 as a highly localized region of low turbulence, unlike simple equilibrium models.

The non-detection of Oph A-N6 as a two-dimensional maximum of $N(H_2)$ but its clear detection as a location of maximal $N(N_2H^+)$ suggest that interesting sites possibly related to star formation may be overlooked in maps of thermal continuum emission. Why was N6 not seen, e.g., by MAN98? Contrasts of $N(H_2)$ in N6 could be minimized if dust at its inner radii are colder than dust at its outer radii (e.g., see Evans et al.), a strong possibility given the high densities and extinctions observed in Oph A. Note, however, that Bouwman, Galli, & André (2004, in preparation; see also André et al. 2003) have recently shown that 1.3 mm continuum flux and T_{dust} are anticorrelated in starless cores, even those with the high column densities and incident radiation fields of Oph A (e.g., 85 G_o; Liseau et al. 1999). The Oph A objects, especially N6, must be specifically modeled to evaluate better this possibility.

If Oph A-N6 is a kernel-like object, we speculate that the Oph A continuum objects may also be or once were kernel-like. In this scenario, the large ΔV of these objects relative to that of Oph A-N6 may suggest that they are now in a state of collapse. For example, N6 has narrow lines close to the thermal line width; an absence of wings or asymmetrically blue profiles in the line suggest that collapse has not yet occurred.[8] If the continuum objects have had similar physical conditions to N6 earlier, turbulence may have been similarly reduced at that epoch. Therefore, their larger ΔV may not be due to substantial turbulent motions in their associated gas. Indeed, how turbulent motions could be reintroduced to these objects after its reduction in the absence of protostars, winds, or outflows is unclear. Instead, gas within these objects may still be thermally dominated and the line broadening observed may be due to infall motions stemming from collapse[9]. The N_2H^+ 1–0 line is only marginally optically thick toward these objects, so the line should remain symmetric, as seen in Figure 5, if emitted from infalling gas (Myers, Evans, & Ohashi 2000). We note here again that SM1, SM1N, and SM2 are found relatively close to (but are not coincident with) positions of the largest ΔV in Oph A; these extreme line widths may also be caused by infall motions related to these objects. Furthermore, the correlation of ΔV vs. V_{LSR} found for bright line emission shown in Fig. 6a may be also related to infall motions. The observed FWZIs of

[8]If N_2H^+ 1–0 has thermalized within N6, and $T_{ex} \approx T_K$, the line will not show infall asymmetry if no gradient in T_{ex} exists.

[9]Belloche et al. (2001; 2004, in preparation) have detected the asymmetrically blue profiles of CS lines that suggest infall toward at least SM2.

N_2H^+ 1–0 toward SM1N, SM1, and SM2 are ∼1.0 km s^{-1}, suggesting infall motions on scales of ∼1000-3000 AU up to 0.5 km s^{-1}, similar to those measured directly toward the Class 0 objects NGC 1333 IRAS 4A and 4B by Di Francesco et al.

Further speculating, we note that the variations of V_{LSR} in Oph A may provide additional evidence for differences in the evolutionary stages of starless objects within Oph A, by supporting the idea that Oph A-N6 is not collapsing but SM1N, SM1, and SM2 may be. N6 appears to have no associated N_2H^+ 1–0 velocity gradients but the continuum objects have small ones (i.e., ≤0.5 km s^{-1} over ∼0.01 pc; see Fig. 3b). Such small velocity gradients could stem from increases in local rotation speeds of dense gas that could accompany inward motions due to angular momentum conservation. (Indeed line broadening by rotational motions may also be contributing to the larger line widths associated with these objects. Note that the gradients in Fig. 3b, however, are seen on scales larger than the beam size.) High-resolution data of Oph A in other tracers of quiescent dense gas that require higher levels of excitation than N_2H^+ 1–0 could reveal velocity gradients more dominated by infall or rotation and clarify this issue (e.g., see Caselli et al. 2002b).

5. Summary and Conclusions

1. Combined single-dish and interferometer data of N_2H^+ 1–0 line emission from Oph A are presented that yield a map of dense gas at high linear resolution (e.g., ∼1000 AU) with information retained on large spatial scales. Six maxima of integrated line intensity, Oph A-N1 through N6, have been detected. N4 and N5 are coincident with the starless objects SM1 and SM1N respectively. The other maxima, however, are not coincident with known starless or protostellar Oph A objects. Moreover, little N_2H^+ 1–0 emission is associated with the starless object SM2 or the Class 0 protostar VLA 1623. This situation is in contrast with observations of isolated cores where dust peaks and integrated N_2H^+ intensity maxima are commonly coincident.

2. With 1.3 mm continuum data from MAN98 and T_{dust} estimates from AWB93, $N(N_2H^+)$, $N(H_2)$, and $X(N_2H^+)$ were estimated for the Oph A objects. SM1 and SM1N have similar values of $X(N_2H^+) \approx$ 2-3 × 10^{-10}. SM2 and VLA 1623, however, have values of $X(N_2H^+)$ that are factors of >4 less than those of SM1 and SM1N. The $X(N_2H^+)$ of Oph A-N6 is similar to that of SM1 and SM1N, if $T_{dust} \approx 15$ K at that location. For SM2 and VLA 1623, the lower values of $X(N_2H^+)$ are likely due to gas-grain chemistry in cold, dense cores where N_2 adsorbs onto grain surfaces and N_2H^+ is depleted, as suggested by many. Similar depletion may not have occurred at SM1 or SM1N because their dust is warmer, e.g., $T_{dust} = 27$ K, perhaps inhibiting N_2 adsoption.

3. N_2H^+ 1–0 line widths (ΔV) in Oph A vary by a factor of $\sim$5 with values $<$0.30 km s^{-1} found in fourteen locations. Of these, only the location associated with the N6 maximum of integrated intensity is both a local minimum of line width and has an extent larger than the beam size. The minimum ΔV in N6 is only 0.193 km s^{-1}, or just larger than line widths expected from thermal motions alone at expected temperatures. In contrast, the ΔV associated with the SM1, SM1N, and SM2 objects are $\sim$0.5 km s^{-1}.

4. N_2H^+ 1–0 line centroids (V_{LSR}) in Oph A vary little across the core, having an rms of only $\sim$0.17 km s^{-1}. No large-scale gradient is seen across Oph A, although small-scale V_{LSR} gradients of $<$0.5 km s^{-1} over 0.01 pc are associated with SM1, SM1N, and SM2, but not with N6. The ΔV and V_{LSR} of Oph A as a whole yield a one-dimensional velocity dispersion, σ, for Oph A that is a factor of $\sim$2 of that required for gravitational virial equilibrium.

5. The low ΔV and lack of V_{LSR} gradient of N6 relative to SM1, SM1N, and SM2 suggest evolutionary differences. The one-dimensional velocity of N6 suggest it alone is within a factor of 2 from gravitational virial equilibrium. N6 has properties (e.g., ΔV, mass, and short proximity to neighbors) similar to those predicted for "kernels", i.e., thermally dominated, critically stable, Bonnor-Ebert spheres embedded within turbulent cores, although some of its properties (e.g., size and no column density maximum) are dissimilar. N6 may represent an early stage of the evolution of dense gas towards star formation where significant local reduction of turbulent motions occurs. The non-detection of N6 in thermal continuum maps of Oph A suggests that interesting sites possibly related to star formation may be missed in such maps.

We thank our referee, Edwin Bergin, for numerous suggestions which improved this paper. In addition, we thank David Wilner, Frederique Motte, Aurore Bacmann, Tamara Helfer, Zhi-Yun Li, Fumitaka Nakamura, and Helmut Weisemeyer for fruitful discussions regarding this project. Furthermore, JD thanks Leo Blitz and the Radio Astronomy Laboratory of the University of California, Berkeley for generous support from a postdoctoral fellowship via the Berkeley-Illinois-Maryland Association.

REFERENCES

Aikawa, Y., Ohashi, N., & Herbst, E. (AOH03) 2003, ApJ, 593, 906

Allen, L. E., Myers, P. C., Di Francesco, J., Mathieu, R. D., Chen, H., & Young, E. 2002, ApJ, 566, 993

André, P., Bouwman, J., Belloche, A., & Hennebelle, P. 2003, in Chemistry as a Diagnostic

of Star Formation, ed. C. L. Curry, & M. Fich, (Ottawa: NRC Press), 127

André, P., Ward-Thompson, D. & Barsony, M. (AWB93) 1993, ApJ, 406, 122

Belloche, A., André, P., & Motte, F. 2001, in "From Darkness to Light," eds. T. Montmerle & P. André, ASP Conf. Ser., 243, p. 313

Benson, P. J., Caselli, P., & Myers P. C. 1998, ApJ, 506, 473

Bergin, E. A., & Langer W. D. 1997, ApJ, 486, 316

Bergin, E. A., Neufeld, D. A., & Melnick, G. J. 1998, ApJ, 499, 777

Bergin, E. A., Alves, J., Huard, T., & Lada, C. J. 2002, ApJ, 570, L101

Bertoldi, F., & McKee, C. F. 1992, ApJ, 395, 140

Bonnell, I. A., Bate, M. R., Clarke, C. J., & Pringle, J. E. 1997, MNRAS, 285, 201

Bonnell, I. A., Bate, M. R., Clarke, C. J., & Pringle, J. E. 2001, MNRAS, 323, 785

Bonnor, W. B. 1956, MNRAS, 116, 351

Buisson, G., Desbats, L., Duvert, G., Forveille, T., Gras, R., Guilloteau, S., Lucas, R., & Valiron, P. 2002, Continuum and Line Analysis Single-dish System Manual, (CLASS; IRAM: Grenoble; http://iram.fr/GS/class/class.html)

Caselli, P., Myers, P. C. & Thaddeus, P. (CMT95) 1995, ApJ, 455, L77

Caselli, P., Benson, P. J., Myers, P. C., & Tafalla, M. 2002a, ApJ, 572, 238

Caselli, P., Walmsley, C. M., Zucconi, A., Tafalla, M., Dore, L., Myers, P. C. 2002b, ApJ, 565, 331

Caselli, P., van der Tak, F. F. S., Ceccarelli, C., & Bacmann, A. 2003, A& A, 403, L37

de Geus, E. J. 1992, A& A, 262, 258

de Geus, E. J., de Zeeuw, P. T., & Lub J. 1989, A& A, 216, 44

Di Francesco, J., Myers, P. C., Wilner, D. J., Ohashi, N., & Mardones, D. 2001, ApJ, 562, 770

Elias, J. H. 1978, ApJ, 224, 453

Evans, N. J., II, Rawlings, J. C., Shirley, Y. L., & Mundy, L. G. 2001, 557, 193

Goodman, A. A., Barranco, J. A., Wilner, D. J., & Heyer, M. R. 1998, ApJ, 504, 223

Green, S., Montgomery, J. A. Jr., & Thaddeus, P. 1974, ApJ, 193, L89

Harju, J., Walmsley, C. M., & Wouterloot, J. G. 1993, A& AS, 98, 51

Jijina, J., Myers, P. C., & Adams, F. C. 1999, ApJS, 125, 161

Kamazaki, T., Saito, M., Hirano, N., Umemoto, T., & Kawabe, R. 2001, ApJ, 584, 357

Kamazaki, T., Saito, M., Hirano, N., & Kawabe, R. 2001, ApJ, 548, 278

Lada, C. J., & Lada, E. A. 2003, ARA& A, 41, 57

Ladd, E. F., Myers, P. C., & Goodman, A. A. 1994, ApJ, 433, 117

Larson, R. B. 1985, MNRAS, 214, 379

Lee, J.-E., Evans, N. J., II, Shirley, Y. L., & Tatematsu, K. 2003, ApJ, 583, 789

Liseau, R., White, G. J., Larsson, B., Sidher, S., Olofsson, G., Kaas, A., Nordh, L., Caux, E., Lorenzetti, D., Molinari, S., Nisini, B., & Sibille, F. 1999, A& A, 344, 342

Looney, L. W., Mundy, L. G. & Welch, W. J. 2000, ApJ, 529, 477

Loren, R. B. 1989a, ApJ, 338, 902

Loren, R. B. 1989b, ApJ, 338, 925

Loren, R. B., Wootten, A., & Wilking B. 1990, ApJ, 365, 269 (LWW90)

McKee, C. F. 1989, ApJ, 345, 782

McKee, C. F., Zweibel, E. G., Goodman, A. A., & Heiles, C. 1993, in Protostars and Planets III, ed. E. Levy, & J. I. Lunine (Tucson: Univ. Arizona Press), 327

Meyer, M. R., Adams, F. C., Hillenbrand, L. A., Carpenter, J. M., & Larson, R. B. 2000, in Protostars and Planets IV, ed. V. Mannings, S. S. Russell, & A. R. Boss, (Tucson: Univ. Arizona Press), 121

Motte, F., André, P. & Neri, R. (MAN98) 1998, AA, 336, 150

Mouschovias, T. Ch. 1991, ApJ, 373, 169

Myers, P. C. 1997, in Star Formation, Near and Far, ed. S. Holt and L. G. Mundy (New York: AIP), 41

Myers, P. C. 1999, ApJ, 496, L109

Myers, P. C., Evans, N. J., & Ohashi, N. 2000, in Protostars and Planets IV, ed. V. Mannings, S. S. Russell, & A. R. Boss, (Tucson: Univ. Arizona Press), 217

Nakano, T. 1998, ApJ, 494, 587

Ohishi, M., Irvine, W., M., & Kaifu N. 1992, in IAU Symposium No. 150, Astrochemistry of Cosmic Phenomena, ed. P. D. Singh, (Dordrecht: Kluwer), 171

Press, W. H., Teukolsky, S. A., Vetterling, W. T., & Flannery, B. P. 1992, Numerical Recipes in FORTRAN, (Cambridge: Cambridge Univ. Press)

Sault, R. J., Teuben, P. J., & Wright M. C. H. 1995, in "Astronomical Data Analysis Software and Systems IV," ed. R.A. Shaw, H.E. Payne and J.J.E. Hayes, (San Francisco: ASP), p. 433.

Shematovich, V. I., Wiebe, D. S., Shustov, B. M., & Li, Z.-Y. 2003, ApJ, 588, 894

Shu, F. H. 1977, ApJ, 214, 488

Steer, D. G., Dewdney, P. E., & Ito, M. R. 1984, AA, 137, 159

Tachihara, K., Mizuno, A., & Fukui, Y. 2000, ApJ, 528, 817

Tafalla, M., Myers, P. C., Caselli, P., Walmsley, C. M., & Comito, C. 2002, ApJ, 569, 815

Troland, T. H., Crutcher, R. M., Goodman, A. A., Heiles, C., Kazès, J., & Myers, P. C. 1996, ApJ, 471, 302

Ungerechts H., et al. 2000, in "Imaging at Radio through Submillimeter Wavelengths," ASP Conf. Ser., Vol. 217, eds. J.G. Mangum & S.J.E. Radford, (San Francisco: ASP), p. 190

van Dishoeck, E. F. & Hogerheijde, M. R. 1999, in The Origin of Stars and Planetary Systems, ed. C. J. Lada, & N. D. Kylafis (Dordrecht: Kluwer), 97

Williams, J. P., Myers, P. C., Wilner, D. J., & Di Francesco, J. 1998, ApJ, 513, L61

Williams, J. P., & Myers, P. C. 2000, ApJ, 537, 891

Womack, M., Ziurys, L. M., & Wyckoff, S. 1992, 387, 417

Zucconi, A., Walmsley, C. M., & Galli, D. 2001, A& A, 376, 650

This preprint was prepared with the AAS LaTeX macros v5.0.

Fig. 1.— a) 1.3 mm continuum emission from Oph A mapped by MAN98 with the IRAM 30 m Telescope. Solid contours start at 100 mJy beam^{-1}, increase in steps of 100 mJy beam^{-1} to 1400 mJy beam^{-1}. The greyscale range shown is 75–2000 mJy beam^{-1}. The 1 σ rms noise level of the map is $\sim$10 mJy beam^{-1}. Significant emission is found at lower levels than indicated by the first contour, but this has been cut here for clarity. The position of the Class 0 protostar VLA 1623 from MAN98 is denoted by a box, and positions of starless objects from MAN98 are denoted by triangles. The position of the near by B star S1 (also E25; Elias 1978) is denoted by a star. The black circle at lower right denotes the relative size of the 13″ map resolution. b) Integrated intensity of N_2H^+ 1–0 line emission from Oph A obtained with the IRAM 30 m Telescope and BIMA interferometer. The values shown are the "zeroth-moment" of CLEANed data, where only intensities exceeding ± 2 σ rms per channel were summed. Solid contours denote 2.8, 8.4, 14.0, 19.7, 25.3, 30.9, 36.5, 42.1, and 47.8 K km s^{-1}, while the dashed contour denotes -2.8 K km s^{-1}. The greyscale range shown is 1.4–65.2 K km s^{-1}. The 1 σ rms noise level over the central mosaic area is 1.4 K km s^{-1}. Symbols are defined as for panel a), except the position of maximum N_2H^+ integrated intensity Oph A-N6 is denoted as an open diamond. Also, the ellipse at lower right here denotes the relative size of the 9.″9 × 6.″1 map resolution.

Fig. 2.— a) Column densities of H_2 obtained using Equation 2 and the 1.3 mm continuum data of MAN98 assuming a constant T_{dust} = 20 K at all locations. The values shown are those derived after binning the MAN98 data first into 13.″5 × 13.″5 pixels (i.e., approximately the beam size of the MAN98 1.3 mm continnum IRAM 30 m data) and then regridding into 6.″75 × 10.″5 pixels (i.e., approximately the beam size of our N_2H^+ line BIMA+IRAM data.) The $N(H_2)$ shown have been divided by 10^{21} cm^{-2}, and the color scale ranges from 0 to 531. Triangles denote the locations of starless continuum objects detected by MAN98, the box denotes the location of VLA 1623, and the diamond denotes the location of Oph A-N6. The white contour displays locations in the N_2H^+ line data where $T_{mb}^{max} \geq 3$ σ. b) Column densities of N_2H^+ obtained using Equation 3 and values of τ_{tot}, T_{ex}, and ΔV obtained from HFS fits. The values shown are those derived after binning the combined data from 0.″5 × 0.″5 pixels into 6.″75 × 10.″5 pixels (i.e., approximately the beam size of the data.) The $N(N_2H^+)$ shown have been divided by 10^{12} cm^{-2} and the color scale ranges from -12 to 125. Symbols and contours are defined as for Figure 3a. c) Fractional abundances of N_2H^+ obtained by assuming $N(H_2)$ is linearly proportional to continuum dust emission and T_{dust} = 20 K for every pixel (see Equation 2). The $X(N_2H^+)$ shown have been divided by 10^{11} and the color scale ranges from 0 to 64. Symbols and contours are defined as for Figure 3a.

Fig. 3.— a) Spatial distribution of the characteristics of N_2H^+ 1–0 from Oph A measured by HFS fitting the combined IRAM and BIMA data. Only results from data where the peak intensity of the brightest hyperfine component equalled or exceeded 3 σ rms are shown.

Symbols are defined as for Figure 1. a) Line width (FWHM) or ΔV. The color scale shown ranges from 0.2 to 0.8 km s^{-1} FWHM. The contours shown begin at 0.15 km s^{-1} and increase in steps of 0.15 km s^{-1} to 0.90 km s^{-1}. b) Line velocity or V_{LSR}. The color scale range shown is 3–4 km s^{-1}. The contours shown begin at 2.8 km s^{-1} and increase in steps of 0.2 km s^{-1} to 4.2 km s^{-1}.

Fig. 4.— The observed spectrum of N_2H^+ 1–0 at the position of minimum line width in Oph A-N6, i.e., at R.A., decl. (2000) = $16^h26^m30.75^s$, -24°24′40″.45 (solid line), together with a spectrum corresponding to its HFS fit (dashed line).

Fig. 5.— Spectral grid of N_2H^+ 101-012 (i.e,. the "isolated" component of N_2H^+ 1–0) over Oph A. Each panel contains a spectrum corresponding to the combined N_2H^+ data averaged into pixels 10″.5 × 6″.75 in size (i.e., approximately the size of the combined beam.) The panels are positioned to correspond to previous images with this pixel sizes, e.g., Figure 3. The abscissa of each panel is V_{LSR} and ranges from 2.0 km s^{-1} to 6.0 km s^{-1}. The ordinate of each panel is T_B and ranges from -3 K to 15 K. Each spectral channel is 0.079 km s^{-1} wide. Triangles, squares, and diamonds are defined as in previous Figures.

Fig. 6.— a) Plot of V_{LSR} vs. Δ_V for N_2H^+ 1–0 in Oph A from HFS fits to combined data in beam-sized pixels, where $T^B_{max} > 9\ \sigma$. The solid line is the linear fit to these data. b) the same quantities as shown in Figure 9a, except the data shown are those from where T^B_{max} is 3–9 σ.

Fig. 7.— Spectra of N_2H^+ 101-012 averaged over various locations in Oph A. *Bold-line* spectra are averages over 2-4 neighboring beam-sized pixels containing the narrowest bright N_2H^+ emission and the *thin-line* spectra are averages over the brightest 4-6 surrounding pixels with weaker, broader emission. Spectra 1 consist of narrow-line emission averaged over 2 pixels in Oph A-N6 or broader-line emission averaged over 4 pixels around Oph A-N6. Spectra 2 consist of narrow-line emission averaged over 3 pixels north of VLA 1623 or east of SM1 or broader-line emission averaged over 7 pixels to the north, west, or south of the narrow-line emission. Spectra 3 consist of narrow-line emission in 4 pixels northwest of SM1N or broader-line emission in 2 pairs of 2 pixels northwest or southeast of the narrow-line emission.

Table 1: Positions of Maximum N_2H^+ 1–0 Integrated Intensity in Oph A

Name	R.A.(2000)	decl. (2000)	Association
N1	16 26 26.4	-24 23 07	A-MM5?
N2	16 26 26.5	-24 22 24	···
N3	16 26 27.2	-24 24 20	···
N4	16 26 27.2	-24 23 50	SM1
N5	16 26 27.4	-24 23 30	SM1N
N6	16 26 31.6	-24 24 52	···

Table 2: N_2H^+ Line Characteristics in Oph A

Value	Unit	mean	rms	min	max
V_{LSR}	km s^{-1}	3.49	0.17	2.98	3.91
ΔV	km s^{-1}	0.39	0.11	0.14	0.88
T_B	K	13.68	3.47	5.25	26.29
τ_{tot}		5.40	3.33	$\leq$0.1	13.05

Table 3: Column Densities and N_2H^+ Abundances in Oph A

Value	Unit	mean	rms	min	max
$N(H_2)$	10^{21} cm^{-2}	179.7	125.3	32.44	530.8
$N(N_2H^+)$	10^{12} cm^{-2}	30.24	27.83	2.675	125.9
$X(N_2H^+)$	10^{-11}	18.61	12.73	1.533	64.34

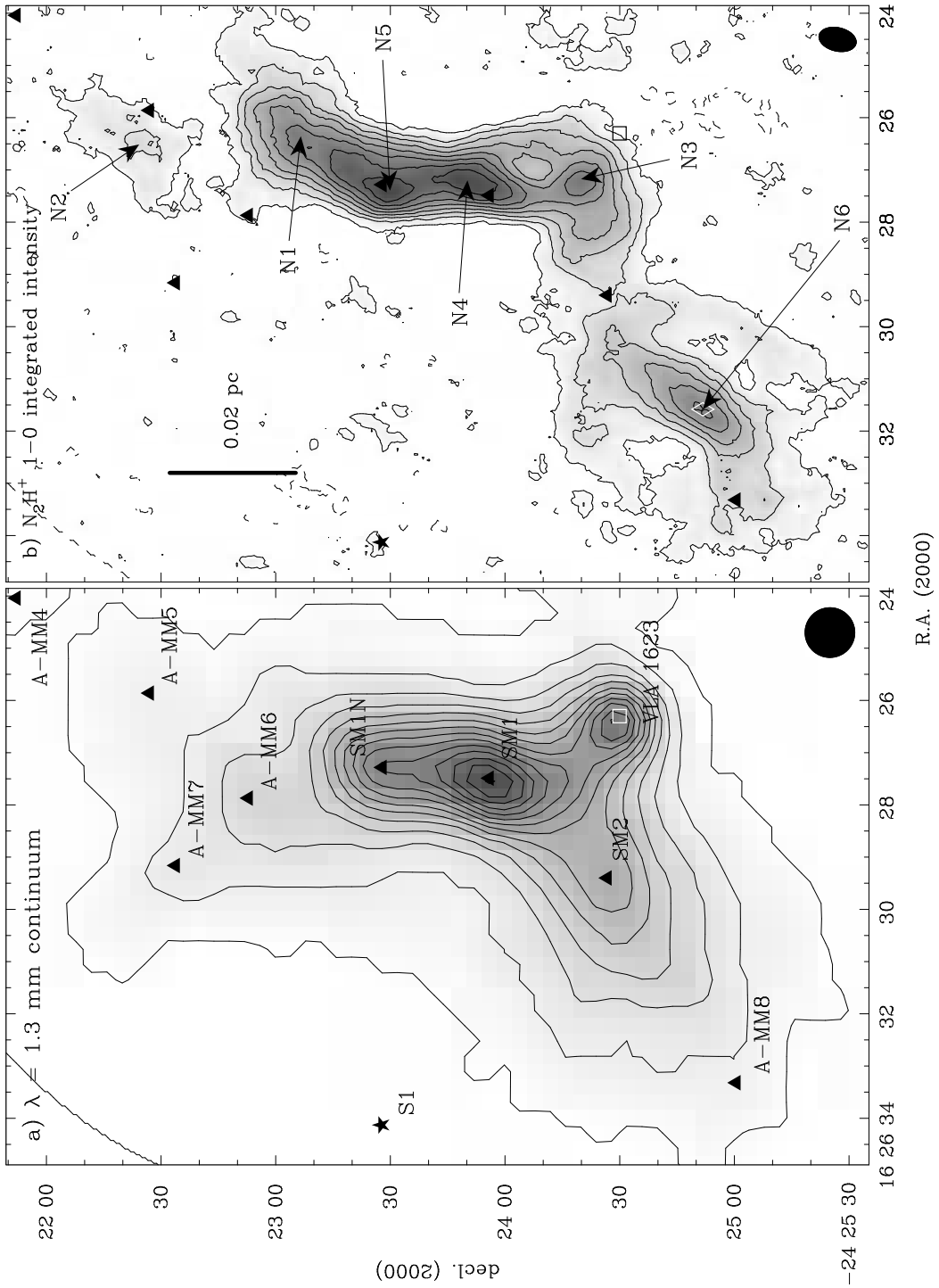
Table 4: N_2H^+ Characteristics of Oph A Objects

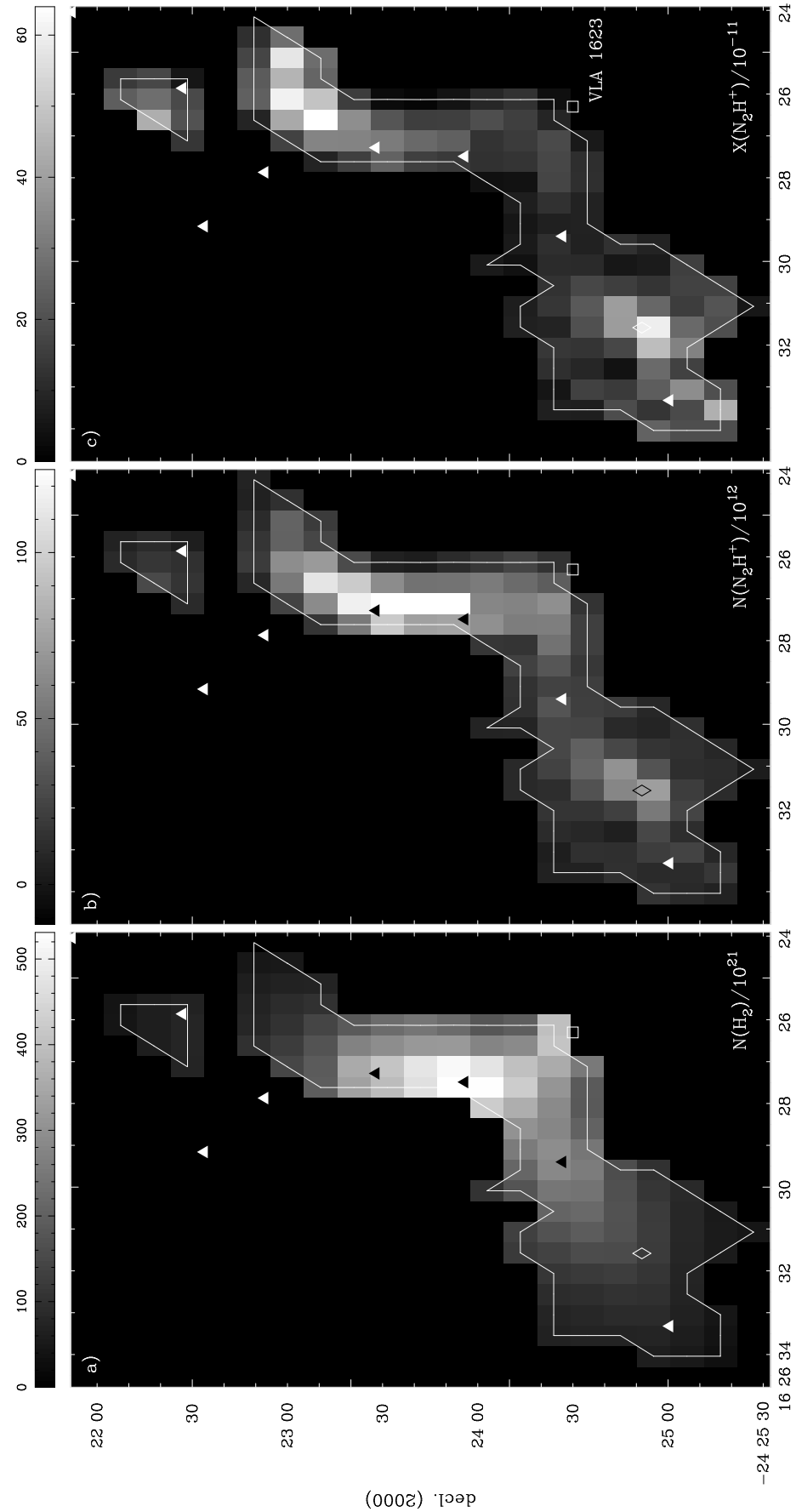
Object	T_{dust}(AWB93) K	$X(N_2H^+)$ $\times10^{-10}$	$N(N_2H^+)$ $\times10^{13}$ cm^{-2}	$N(H_2)$[1] $\times10^{23}$ cm^{-2}	$\Delta V(N_2H^+)$ km s^{-1}	V_{LSR} km s^{-1}
VLA 1623	15-20	<0.4–<0.7	<3	6-4	···	···
SM1N	27	3	10	3	0.49	3.60
SM1	27	2	8	4	0.59	3.72
SM2	<20	<0.9	2	>3	0.52	3.47
Oph A-N6	15?	4	6	3	0.25	3.47

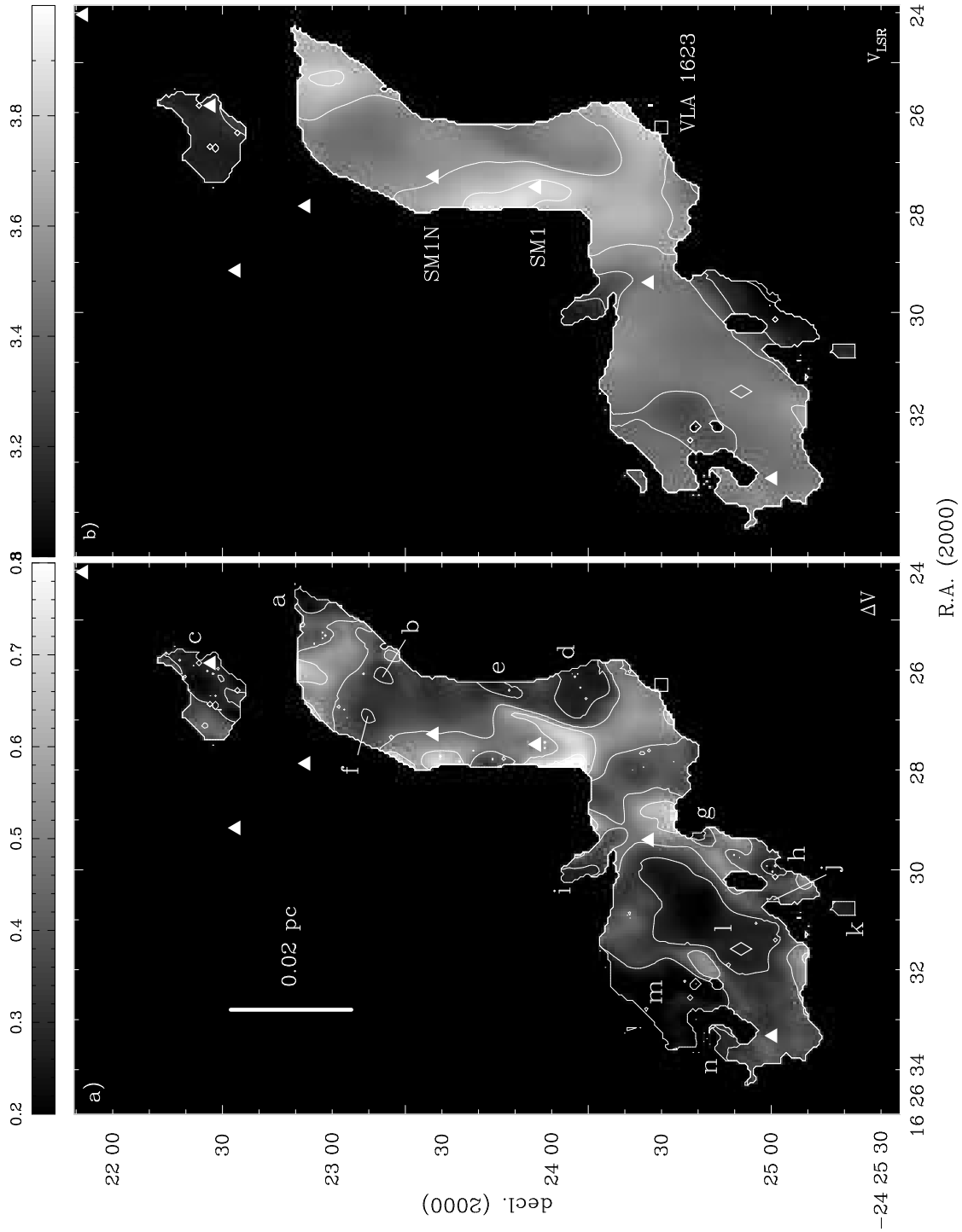
[1] $N(H_2)$ values were derived assuming all continuum emission detected along the lines-of-sight are associated with the objects in question. Since Oph A-N6 is not an peak of continuum emission like the other objects here, its $N(H_2)$ may be overestimated.

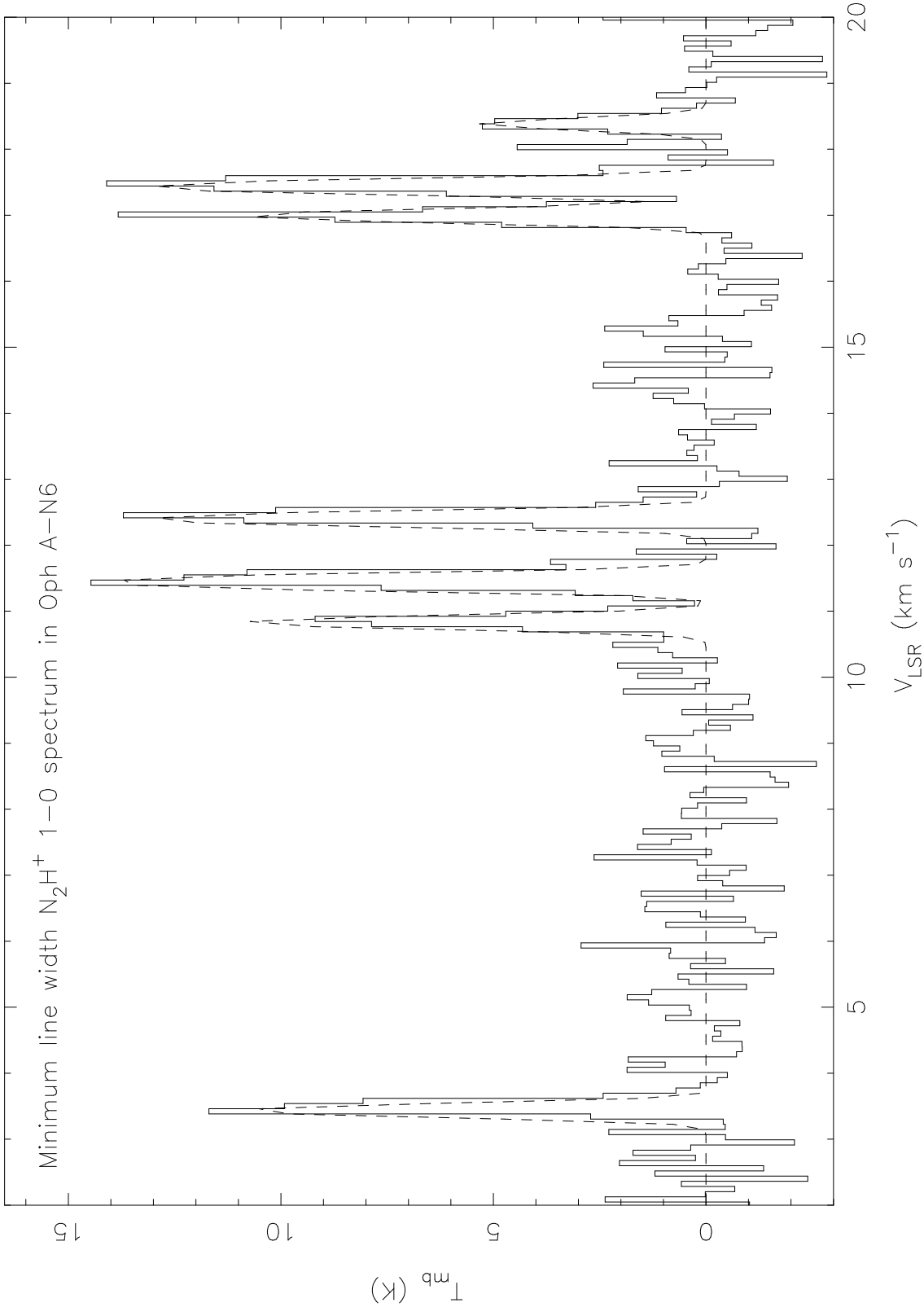
Table 5: Positions in Oph A of N_2H^+ 1–0 $\Delta V < 0.30$ km s^{-1}

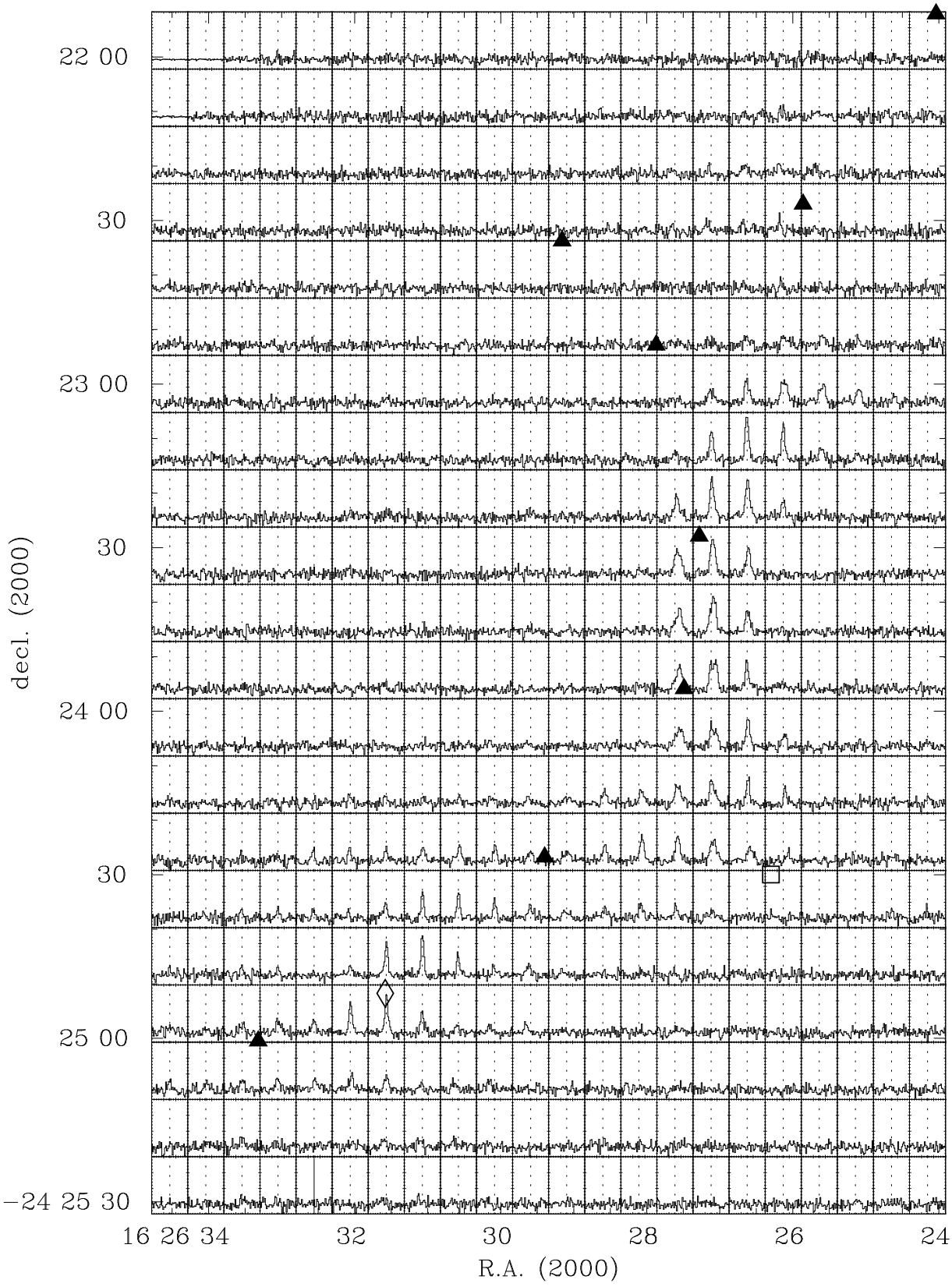
Name	R.A.(2000)	decl. (2000)	ΔV	Association
a	16 26 24.8	-24 22 54	0.24	···
b	16 26 26.1	-24 23 14	0.29	N1
c	16 26 26.3	-24 22 24	0.26	N2
d	16 26 26.3	-24 24 08	0.27	···
e	16 26 26.4	-24 23 48	0.28	···
f	16 26 26.9	-24 23 10	0.29	···
g	16 26 29.3	-24 24 40	0.27	N1
h	16 26 30.0	-24 25 01	0.28	···
i	16 26 30.1	-24 24 05	0.28	···
j	16 26 30.6	-24 25 01	0.29	···
k	16 26 30.7	-24 24 40	0.27	···
l	16 26 30.7	-24 25 20	0.26	N6
m	16 26 32.4	-24 24 33	0.21	···
n	16 26 33.4	-24 24 48	0.29	···

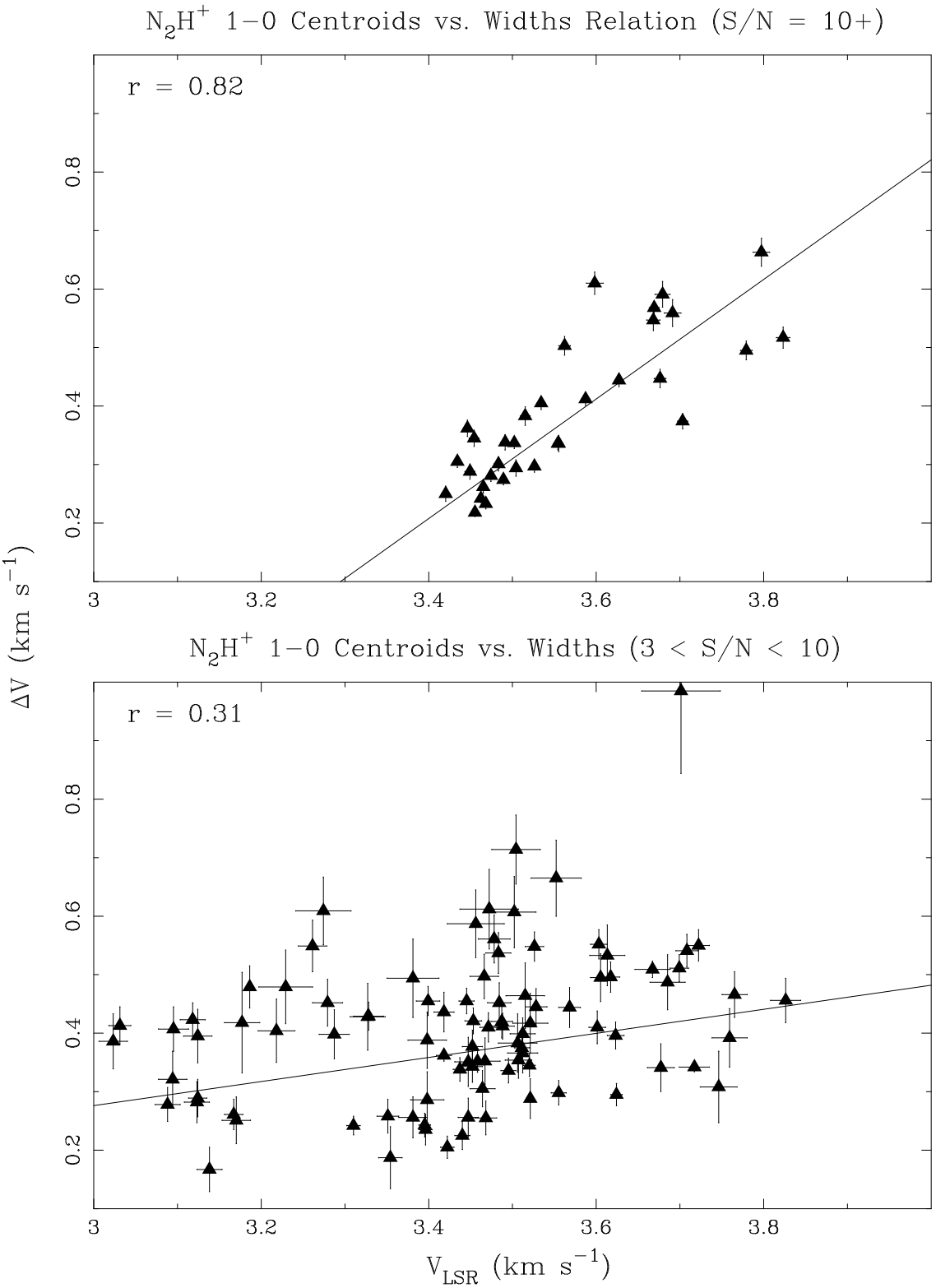

a) λ = 1.3 mm continuum
A−MM4
A−MM5
A−MM6
A−MM7
A−MM8
SM1N
SM1
SM2
VLA 1623
S1
b) N_2H^+ 1−0 integrated intensity
N1
N2
N3
N4
N5
N6
0.02 pc
22 00
30
23 00
30
24 00
30
25 00
30
−24 25 30
16 26 34
32
28
26
24
decl. (2000)
R.A. (2000)

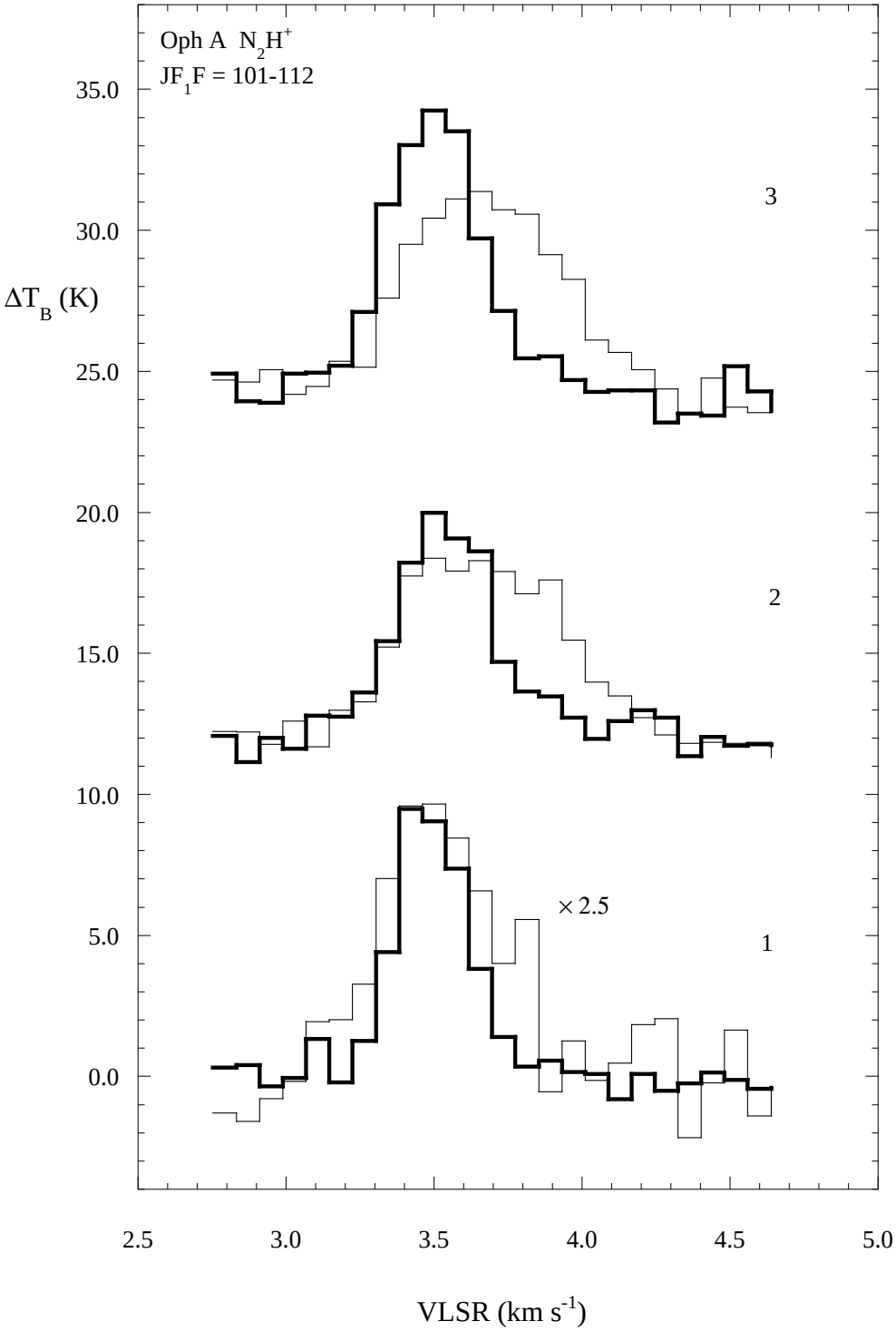

a)
b)
c)
$N(H_2)/10^{21}$
$N(N_2H^+)/10^{12}$
$X(N_2H^+)/10^{-11}$
VLA 1623
R.A. (2000)
decl. (2000)
16 26 34
32
30
28
26
24
−24 25 30
25 00
24 00
23 00
22 00


a)
b)
0.02 pc
ΔV
V_{LSR}
SM1N
SM1
VLA 1623
a
b
c
d
e
f
g
h
i
j
k
l
m
n
0.2
0.3
0.4
0.5
0.6
0.7
0.8
3.2
3.4
3.6
3.8
22 00
30
23 00
30
24 00
30
25 00
−24 25 30
16 26 34
32
30
28
26
24
32
30
28
26
24
decl. (2000)
R.A. (2000)


Minimum line width N_2H^+ 1–0 spectrum in Oph A–N6
T_{mb} (K)
0
5
10
15
V_{LSR} (km s^{-1})
5
10
15
20


22 00
30
23 00
30
24 00
30
25 00
−24 25 30
decl. (2000)
16 26 34
32
30
28
26
24
R.A. (2000)


N_2H^+ 1−0 Centroids vs. Widths Relation (S/N = 10+)
r = 0.82
N_2H^+ 1−0 Centroids vs. Widths (3 < S/N < 10)
r = 0.31
ΔV (km s^{-1})
V_{LSR} (km s^{-1})
0.2
0.4
0.6
0.8
3
3.2
3.4
3.6
3.8


Oph A N2H+
JF1F = 101-112
35.0
30.0
25.0
20.0
15.0
10.0
5.0
0.0
ΔTB (K)
3
2
1
× 2.5
2.5
3.0
3.5
4.0
4.5
5.0
VLSR (km s-1)